

**1 Statistical state dynamics of weak jets in barotropic beta-plane turbulence**

**2 Nikolaos A. Bakas**

**3 *Laboratory of Meteorology and Climatology, Department of Physics, University of Ioannina,***  
**4 *Ioannina, Greece***

**5 Navid C. Constantinou\***

**6 *Scripps Institution of Oceanography, University of California San Diego, La Jolla, California,***  
**7 *USA***

**8 *Research School of Earth Sciences, Australian National University, Canberra, ACT, 2601,***  
**9 *Australia***

**10 *ARC Centre of Excellence for Climate Extremes, Australian National University, Canberra, ACT,***  
**11 *2601, Australia***

**12 Petros J. Ioannou**

**13 *Department of Physics, National and Kapodistrian University of Athens, Athens, Greece***

**14 \*Corresponding author address:** Navid Constantinou, 142 Mills Road, Building Jaeger 8, Research

**15 School of Earth Sciences, Australian National University, Canberra, ACT, 2601, Australia.**

**16 E-mail:** navid.constantinou@anu.edu.au

## ABSTRACT

17 Zonal jets in a barotropic setup emerge out of homogeneous turbulence through a flow-forming instability of the homogeneous turbulent state  
18 ('zonostrophic instability') which occurs as the turbulence intensity increases.  
19  
20 This has been demonstrated using the statistical state dynamics (SSD) framework with a closure at second order. Furthermore, it was shown that for small  
21 supercriticality the flow-forming instability follows Ginzburg–Landau (G–L)  
22 dynamics. Here, the SSD framework is used to study the equilibration of this  
23 flow-forming instability for small supercriticality. First, we compare the predictions of the weakly nonlinear G–L dynamics to the fully nonlinear SSD  
24 dynamics closed at second order for a wide ranges of parameters. A new  
25 branch of jet equilibria is revealed that is not contiguously connected with  
26 the G–L branch. This new branch at weak supercriticalities involves jets with  
27 larger amplitude compared to the ones of the G–L branch. Furthermore, this  
28 new branch continues even for subcritical values with respect to the linear  
29 flow-forming instability. Thus, a new *nonlinear* flow-forming instability out  
30 of homogeneous turbulence is revealed. Second, we investigate how both the  
31 linear flow-forming instability and the novel nonlinear flow-forming instability  
32 are equilibrated. We identify the physical processes underlying the jet  
33 equilibration as well as the types of eddies that contribute in each process.  
34  
35 Third, we propose a modification of the diffusion coefficient of the G–L dy-  
36 namics that is able to capture the evolution of weak jets at scales other than the  
37 marginal scale (side-band instabilities) for the linear flow-forming instability.  
38

39 **1. Introduction**

40 Robust eddy-driven zonal jets are ubiquitous in planetary atmospheres (Ingersoll 1990; Inger-  
41 soll et al. 2004; Vasavada and Showman 2005). Laboratory experiments, theoretical studies, and  
42 numerical simulations show that small-scale turbulence self-organizes into large-scale coherent  
43 structures, which are predominantly zonal and, furthermore, that the small-scale turbulence sup-  
44 ports the jets against eddy mixing (Starr 1968; Huang and Robinson 1998; Read et al. 2007; Salyk  
45 et al. 2006). One of the simplest models, which is a testbed for theories regarding turbulence  
46 self-organization, is forced-dissipative barotropic turbulence on a beta-plane.

47 An advantageous framework for understanding coherent zonal jet self-organization is the study  
48 of the Statistical State Dynamics (SSD) of the flow. SSD refers to the dynamics that governs the  
49 statistics of the flow rather than the dynamics of individual flow realizations. However, evolving  
50 the hierarchy of the flow statistics of a nonlinear dynamics soon becomes intractable; a turbulence  
51 closure is needed. Unlike the usual paradigm of homogeneous isotropic turbulence, when strong  
52 coherent flows coexist with the incoherent turbulent field, the SSD of the turbulent flow is well  
53 captured by a second-order closure (Farrell and Ioannou 2003, 2007, 2009; Tobias et al. 2011;  
54 Srinivasan and Young 2012; Bakas and Ioannou 2013a; Tobias and Marston 2013; Constantinou  
55 et al. 2014a,b; Thomas et al. 2014; Ait-Chaala et al. 2016; Constantinou et al. 2016; Farrell et al.  
56 2016; Farrell and Ioannou 2017; Fitzgerald and Farrell 2018a; Frishman and Herbert 2018). Such a  
57 second-order closure comes in the literature under two names: ‘S3T’, which stands for Stochastic  
58 Structural Stability Theory (Farrell and Ioannou 2003) and ‘CE2’, which stands for Cumulant  
59 Expansion of second order (Marston et al. 2008). Hereafter, we refer to this second-order closure  
60 as S3T.

Using the S3T second-order closure it was first theoretically predicted that zonal jets in barotropic beta-plane turbulence emerge spontaneously out of a background of homogeneous turbulence through an *instability of the SSD* (Farrell and Ioannou 2007; Srinivasan and Young 2012). That is, S3T predicts that jet formation is a bifurcation phenomenon, similar to phase transitions, that appears as the turbulence intensity crosses a critical threshold. This prediction comes in contrast with the usual theories for zonal jet formation that involve anisotropic arrest of the inverse energy cascade at the Rhines' scale (Rhines 1975; Vallis and Maltrud 1993). Jet emergence as a bifurcation was subsequently confirmed by comparison of the analytic predictions of the S3T closure with direct numerical simulations (Constantinou et al. 2014a; Bakas and Ioannou 2014). This flow-forming SSD instability is markedly different from hydrodynamic instability in which the perturbations grow in a fixed mean flow. In the flow-forming instability, both the coherent mean flow and the incoherent eddy field are allowed to change. The instability manifests as follows: a weak zonal flow that is inserted in an otherwise homogeneous turbulent field, organizes the incoherent fluctuations to *coherently* reinforce the zonal flow. This instability has analytic expression only in the SSD and we therefore refer to this new kind of instabilities as ‘SSD instabilities’. In particular, the flow-forming ‘SSD instability’ of the homogeneous turbulent state to zonal jet mean flow perturbations is also referred to as ‘zonostrophic instability’ (Srinivasan and Young 2012).

Kraichnan (1976) suggested that the large-scale mean flow is supported by small-scale eddies. Indeed, when the large scales dominate the eddy field (i.e., when the large-scale shear time,  $\tau_m$ , is far shorter than the eddy turnover time,  $\tau_e$ ) the small-scale eddies have the tendency to flux momentum and support large-scale mean flows (Shepherd 1987; Huang and Robinson 1998; Chen et al. 2006; Holloway 2010; Frishman and Herbert 2018). Under such circumstances, we expect the S3T second-order closure of the SSD to be accurate. Furthermore, Bouchet et al. (2013) provided a rigorous proof that in the limit  $\tau_e/\tau_m \rightarrow \infty$  the SSD of large-scale jets in equilibrium

with their eddy field are governed exactly by a second-order closure. Recent studies revealed that the second-order closure remains accurate even at moderate scale separation between  $\tau_m$  and  $\tau_e$  (see, e.g., Srinivasan and Young (2012); Marston et al. (2014, 2016); Frishman et al. (2017); Frishman and Herbert (2018)). That is, the second-order closure manages to reproduces fairly accurately the structure of the mean flow *even though* there could be differences in the eddy spectra and the concomitant eddy correlations; see, e.g., figure 1.

However, surprisingly enough, S3T *remains accurate even at a perturbative level*, i.e., when the mean flows/jets are just emerging with  $\tau_e/\tau_m \rightarrow 0$  (the exactly opposite limit of Bouchet et al. (2013)). This perturbative-level agreement is reported by Constantinou et al. (2014a); Bakas and Ioannou (2013a, 2014) for barotropic flows, by Bakas and Ioannou (2018) for baroclinic flows, by Fitzgerald and Farrell (2018a) for vertically sheared stratified flows, by Constantinou and Parker (2018) for magnetized flows in astrophysical settings, and by Farrell et al. (2017) for the formation of spanwise varying mean flows and mean vortices (streaks–rolls) in 3D channel flows. The reason that the S3T second-order closure works well *even for very weak mean flows* should be attributed to the existence of the collective flow-forming instability which seems to overpower the disruptive eddy–eddy nonlinear interactions, as long as the turbulent intensity is not exceptionally strong (which in most physical situations is usually the case).

The dynamics that underlie the flow-forming SSD instability of the homogeneous state is well understood; Bakas and Ioannou (2013b) and Bakas et al. (2015) studied in detail this eddy–mean flow dynamics for barotropic flows and Fitzgerald and Farrell (2018b) for stratified flows. In these studies, the structures of the eddy field that produce up-gradient momentum fluxes, and thus drive the instability, were determined in the appropriate limit  $\tau_{\text{diss}}/\tau_m \rightarrow 0$ , with  $\tau_{\text{diss}}$  the dissipation time-scale.

108 While the processes by which the flow-forming instability manifests are well understood, we  
109 lack comprehensive understanding of how this instability is equilibrated. For example, as the  
110 zonal jets grow they often merge or branch to larger or smaller scales (Danilov and Gurarie 2004;  
111 Manfroi and Young 1999), multiple turbulence–jet equilibria exist (Farrell and Ioannou 2007;  
112 Parker and Krommes 2013; Constantinou et al. 2014a), and, also, transitions from various turbulent  
113 jet attractors may occur (Simonnet and Bouchet 2016). Some outstanding questions include:

- 114 (i) How is the equilibration of the flow-forming instability achieved and at which amplitude for  
115 the given parameters?
- 116 (ii) What are the eddy–mean flow dynamics involved in the equilibration process as well as  
117 which eddies support the finite amplitude jets?
- 118 (iii) What type of instabilities are involved in the observed jet variability phenomenology (jet  
119 merging and branching, multiple jet equilibria, transitions between various jet attractors) and  
120 what are the eddy–mean flow dynamics involved?

121 To tackle these questions, Parker and Krommes (2013) first pointed out the analogy of jet for-  
122 mation and pattern formation (Hoyle 2006; Cross and Greenside 2009). Exploiting this analogy  
123 Parker and Krommes (2014) were able to borrow tools and methods from pattern formation theory  
124 to elucidate the equilibration process. In particular, they demonstrated that at small supercriti-  
125 cality, that is when the turbulence intensity is just above the critical threshold for jet formation,  
126 the nonlinear evolution of the zonal jets follows Ginzburg–Landau (G–L) dynamics. In addition,  
127 Parker and Krommes (2014) examined the quantitative accuracy of the G–L approximation by  
128 comparison with turbulent jet equilibria obtained from the fully nonlinear S3T dynamics. Having  
129 established the validity of S3T dynamics even in the limit of very weak mean flows/jets (as we have  
130 discussed above), it is natural to then proceed studying the G–L dynamics of this flow-forming in-

131 stability and its associated equilibration process. The perturbative-level agreement of the S3T  
132 predictions with direct numerical simulations of the full nonlinear dynamics argues that the study  
133 of the equilibration of the flow-forming instability using the G–L dynamics is well founded.

134 In this work, we revisit the small-supercriticality regime of Parker and Krommes (2014). We  
135 thoroughly test the validity of the G–L approximation through a comparison with the fully non-  
136 linear SSD closed at second order for a wide range parameter values (section 5). Apart from the  
137 equilibrated flow-forming instability of the homogeneous turbulent state, which is governed by  
138 the G–L dynamics, we discover that an additional branch of jet equilibria exists for large values of  
139  $\beta/(k_f r)$  ( $\beta$  is the planetary vorticity gradient,  $r = 1/\tau_{\text{diss}}$  is the linear dissipation rate, and  $1/k_f$   
140 is the length scale of the forcing). This new branch of equilibria reveals that jets emerge as a  
141 cusp bifurcation, which implies that for large  $\beta/(k_f r)$  the emergent jets result from a nonlinear  
142 instability (see Fig 6(a)).

143 We investigate the eddy–mean flow dynamics involved in the equilibration of the flow-forming  
144 instabilities, as well as those involved in the secondary side-band jet instabilities that occur (sec-  
145 tion 6). To do this, we derive the G–L equation in a physically intuitive way that allows for the  
146 comprehensive understanding of the nonlinear Landau term involved in the G–L equation (sec-  
147 tion 4). Using methods similar to the ones developed by Bakas and Ioannou (2013b) and Bakas  
148 et al. (2015) we study the contribution of the forced eddies and their interactions in supporting  
149 the equilibrated finite amplitude jets (section 6). Finally, to elucidate the equilibration of the new  
150 branch of jet equilibria that are not governed by the G–L dynamics, we develop an alternative  
151 reduced dynamical system which generalizes the G–L equation (section 6b). Using this reduced  
152 system we study the physical processes responsible for the equilibration of the new branch of jet  
153 equilibria.

154 **2. Statistical state dynamics of barotropic  $\beta$ -plane turbulence in the S3T second-order clo-**  
 155 **sure**

156 Consider a non-divergent flow  $\mathbf{u}_* = (u_*, v_*)$  on a  $\beta$ -plane with coordinates  $\mathbf{x}_* = (x_*, y_*)$ ;  $x_*$  is  
 157 the zonal direction and  $y_*$  the meridional direction. Subscript asterisks here denote dimensional  
 158 variables. The flow is in an unbounded domain, unless otherwise indicated. The flow is derived  
 159 from a streamfunction  $\psi_*$  via  $(u_*, v_*) = (-\partial_{y_*} \psi_*, \partial_{x_*} \psi_*)$ . The relative vorticity of the flow is  
 160  $\zeta_* \stackrel{\text{def}}{=} \partial_{x_*} v_* - \partial_{y_*} u_* = \Delta_* \psi_*$ , with  $\Delta_* \stackrel{\text{def}}{=} \partial_{x_*}^2 + \partial_{y_*}^2$  the Laplacian. With stochastic excitation and  
 161 linear dissipation the relative vorticity evolves according to:

$$(\partial_{t_*} + \mathbf{u}_* \cdot \nabla_*)(\zeta_* + \beta_* y_*) = -r_* \zeta_* + \sqrt{\varepsilon_*} \xi_* . \quad (1)$$

162 Linear dissipation at the rate  $r_*$  parametrizes Ekman drag at the surface of the planet. Turbulence is  
 163 supported by the random stirring  $\xi_*(\mathbf{x}_*, t_*)$  that injects energy in the flow at rate  $\varepsilon_*$ . This random  
 164 stirring models vorticity sources such as convection and/or baroclinic growth processes that are  
 165 absent in barotropic dynamics. The random process  $\xi_*$  is assumed (i) to have zero mean, (ii) to be  
 166 spatially and temporally statistically homogeneous, and (iii) to be temporally delta-correlated but  
 167 spatially correlated. Thus it satisfies:

$$\langle \xi_*(\mathbf{x}_*, t_*) \rangle = 0 \quad \text{and} \quad \langle \xi_*(\mathbf{x}_{a*}, t_{*1}) \xi_*(\mathbf{x}_{b*}, t_{*2}) \rangle = Q_*(\mathbf{x}_{a*} - \mathbf{x}_{b*}) \delta(t_{1*} - t_{2*}) , \quad (2)$$

168 with  $Q_*$  the homogeneous spatial covariance of the forcing. Angle brackets denote ensemble  
 169 averaging over realizations of the forcing. The forcing covariance is constructed by specifying a  
 170 non-negative spectral power function  $\hat{Q}_*(\mathbf{k}_*)$  as:

$$Q_*(\mathbf{x}_{a*} - \mathbf{x}_{b*}) = \int \frac{d^2 \mathbf{k}_*}{(2\pi)^2} \hat{Q}_*(\mathbf{k}_*) e^{i \mathbf{k}_* \cdot (\mathbf{x}_{a*} - \mathbf{x}_{b*})} . \quad (3)$$

171 In this work, we consider isotropic forcing with spectrum:

$$\hat{Q}_*(\mathbf{k}_*) = 4\pi k_{f*} \delta(k_* - k_{f*}) , \quad (4)$$

<sup>172</sup> where  $k_* \stackrel{\text{def}}{=} |\mathbf{k}_*|$ . The forcing (4) excites equally all waves with total wavenumber  $k_{f*}$ . The forcing  
<sup>173</sup> spectrum is normalized so that the total energy injection is  $\varepsilon_*$ .<sup>1</sup>

<sup>174</sup> Equation (1) is non-dimensionalized using the forcing length scale  $k_{f*}^{-1}$  and the dissipation time  
<sup>175</sup> scale  $r_*^{-1}$ . The non-dimensional variables are:  $\zeta = \zeta_*/r_*$ ,  $\mathbf{u} = \mathbf{u}_*/(k_{f*}^{-1} r_*)$ ,  $\xi = \xi_*/(k_{f*} \sqrt{r_*})$ ,  
<sup>176</sup>  $\varepsilon = \varepsilon_*/(k_{f*}^{-2} r_*^3)$ ,  $\beta = \beta_*/(k_{f*} r_*)$  and  $r = 1$ . Thus, the non-dimensional version of (1) lacks all  
<sup>177</sup> asterisks and has  $r = 1$ . The non-dimensional form of  $\hat{Q}_*$  in (4) is obtained dropping the asterisks  
<sup>178</sup> and replacing  $k_{f*} \mapsto 1$ .

<sup>179</sup> The statistical state dynamics (SSD) of zonal jet formation in the S3T second-order closure com-  
<sup>180</sup> prise the dynamics of the first cumulant of the vorticity field  $\bar{\zeta}(\mathbf{x}, t)$ , and of the second cumulant  
<sup>181</sup>  $C(\mathbf{x}_a, \mathbf{x}_b, t) \stackrel{\text{def}}{=} \overline{\zeta'(\mathbf{x}_a, t)\zeta'(\mathbf{x}_b, t)}$ .

<sup>182</sup> The overbars here denote zonal average, while dashes denote fluctuations about the mean. Thus,  
<sup>183</sup>  $\bar{\zeta} = -\partial_y \bar{u}$  and, the first cumulant of the flow can be equivalently described with  $\bar{u}$ . Also, the eddy  
<sup>184</sup> covariance  $C$  is therefore homogeneous in  $x$ :  $C(x_a - x_b, y_a, y_b, t)$ . Furthermore, the zonal average  
<sup>185</sup> is assumed to satisfy the ergodic property, i.e., that the average of any quantity is equal to an  
<sup>186</sup> ensemble average over realizations of  $\xi$ :  $\overline{(\cdot)} = \langle (\cdot) \rangle$ .

<sup>187</sup> After dropping terms involving the third cumulant we can form the closed system for the evolu-  
<sup>188</sup> tion of the first and second cumulants of the flow:

$$\partial_t \bar{u} = \mathcal{R}(C) - \bar{u} , \quad (5a)$$

$$\partial_t C = -\mathcal{L}C + \mathcal{N}(\bar{u}, C) + \varepsilon Q . \quad (5b)$$

<sup>189</sup> The derivation of (5) has been presented many times; the reader is referred to, e.g., the work  
<sup>190</sup> by Farrell and Ioannou (2003); Srinivasan and Young (2012); Bakas et al. (2015). In (5),  $\mathcal{L}$   
<sup>191</sup> is the operator given in (A1) that governs the linear eddy dynamics, and  $\mathcal{N}$  is the nonlinear

---

<sup>1</sup>In numerical simulations, we approximate the delta-function in (4) as a gaussian with narrow width—see section 5 for more details.

192 operator given in (A2) that governs the interaction between the eddies and the instantaneous mean  
193 flow  $\bar{u}(y, t)$ . The mean flow  $\bar{u}$  is driven by the ensemble mean eddy vorticity flux  $\overline{v' \zeta'}$ , which  
194 is expressed as a linear function of the eddy vorticity covariance  $C$  through  $\mathcal{R}(C)$  with  $\mathcal{R}$  given  
195 in (A3).

196 The mean flow energy density,  $E_m$ , and the eddy energy density,  $E_p$ , are:

$$E_m = \int_{\infty} d^2x \frac{1}{2} \bar{u}^2, \quad (6a)$$

$$E_p = \int_{\infty} d^2x \frac{1}{2} [\overline{\mathbf{u}'(\mathbf{x}_a) \cdot \mathbf{u}'(\mathbf{x}_b)}]_{\mathbf{x}_a=\mathbf{x}_b} = - \int_{\infty} d^2x \frac{1}{4} [(\Delta_a^{-1} + \Delta_b^{-1}) C]_{\mathbf{x}_a=\mathbf{x}_b}. \quad (6b)$$

197 where  $\int_{\infty} \stackrel{\text{def}}{=} \lim_{L \rightarrow \infty} (2L)^{-2} \int_{-L}^L \int_{-L}^L$ , the subscripts on the Laplacian indicate the specific variable  
198 the operator is acting, and subscript  $a = b$  implies that the function of  $\mathbf{x}_a$  and  $\mathbf{x}_b$ , e.g., inside the  
199 square brackets on the right-hand-side of (6), is transformed into a function of a single variable by  
200 setting  $\mathbf{x}_a = \mathbf{x}_b = \mathbf{x}$ . The total averaged energy density relaxes over the dissipation scale (which  
201 is of  $O(1)$  in the non-dimensional equations) to the energy supported under stochastic forcing and  
202 dissipation:

$$E(t) \stackrel{\text{def}}{=} E_m(t) + E_p(t) = \left[ E(0) - \frac{\epsilon}{2} \right] e^{-2t} + \frac{\epsilon}{2}. \quad (7)$$

203 Therefore, the total energy remains bounded under S3T dynamics (Bakas and Ioannou 2019).

### 204 3. The flow-forming instability and the underlying eddy–mean flow dynamics

205 S3T dynamics under homogeneous stochastic forcing admit, for all parameter values, a homo-  
206 geneous equilibrium with zero mean flow and homogeneous eddy covariance:

$$\bar{u}^e = 0, \quad C^e(\mathbf{x}_a - \mathbf{x}_b) = \frac{\epsilon}{2} Q(\mathbf{x}_a - \mathbf{x}_b). \quad (8)$$

207 The homogeneous equilibrium state (8) becomes unstable at certain parameter values and bifur-  
208 cates to inhomogeneous equilibria, a class of which are zonal jets. The stability of the homoge-

209 neous state (8) is addressed by linearizing (5) around (8). Since (8) is homogeneous, the eigenfunc-  
210 tions consist of a sinusoidal mean flow perturbation  $\delta\bar{u}e^{\sigma t}$  and a perturbation covariance  $\delta C e^{\sigma t}$   
211 with a sinusoidal inhomogeneous part:

$$\delta\bar{u} = e^{iny}, \quad \delta C = \tilde{C}_n^{(h)}(\mathbf{x}_a - \mathbf{x}_b) e^{in(y_a + y_b)/2}, \quad (9)$$

212 where  $n$  is a real wavenumber that indicates the length-scale of the jets. The corresponding eigen-  
213 values  $\sigma$  satisfy (see Appendix A):

$$\sigma + 1 = f(\sigma | \delta\bar{u}, C^e) = \varepsilon f(\sigma | \delta\bar{u}, Q/2), \quad (10)$$

214 where  $f$  is the vorticity flux induced by the distortion of the eddy equilibrium field  $C^e$  by the mean  
215 flow  $\delta\bar{u}$ ; the expression for  $f$  is given in (A9). This induced vorticity flux is referred to as the  
216 *vorticity flux feedback on  $\delta\bar{u}$* . For the ring forcing considered in this study, the fastest growing  
217 instability for  $n < 1$  has a real eigenvalue  $\sigma$  and, therefore, the emergent jets are not translating in  
218 the  $y$  direction. The vorticity flux feedback at marginal stability

$$f_r \stackrel{\text{def}}{=} \text{Re}[f(\sigma = 0 | \delta\bar{u}, Q/2)], \quad (11)$$

219 that is positive in this case, has the tendency to reinforce the preexisting jet perturbation  $\delta\bar{u}$  and  
220 therefore destabilizes it. With dissipation, the critical parameter  $\varepsilon$  at which the homogeneous  
221 equilibrium becomes unstable to a jet with wavenumber  $n$  is  $\varepsilon_t(n) = 1/f_r$  and for all values of  $\beta$   
222 there is a minimum energy input rate

$$\varepsilon_c \stackrel{\text{def}}{=} \min_n [\varepsilon_t(n)], \quad (12)$$

223 above which the homogeneous state is unstable and jet formation occurs.

224 It is instructive to identify which wave components (of the incoherent flow) contribute to the  
225 instability process. For the forcing spectrum (4) we may express the vorticity flux feedback at the

226 stability boundary ( $\sigma = 0$ ) as

$$f_r = \int_0^{\pi/2} \mathcal{F}(\vartheta, n) d\vartheta, \quad (13)$$

227 where  $\mathcal{F}(\vartheta, n)$  is the contribution to  $f_r$  from the wave components with wavevectors  $k =$   
228  $(\pm \cos \vartheta, \pm \sin \vartheta)$  when the homogeneous equilibrium is perturbed by a jet perturbation with  
229 wavenumber  $n$ . Angle  $\vartheta$  measures the inclination of the wave phase lines with respect to the  
230  $y$ -axis. The precise expression for  $\mathcal{F}(\vartheta, n)$  is given in (A12). Positive values of  $\mathcal{F}$  indicate that  
231 waves with phase lines inclined at angle  $|\vartheta|$  produce up-gradient vorticity fluxes that are destabiliz-  
232 ing the jet perturbation  $n$ . In general, destabilizing vorticity fluxes are produced by waves with  
233 phase lines closely aligned to the  $y$ -axis (with small  $|k_y|$ ) as shown in Fig. 2.

234 Figures 3(a) and 3(b) show the contribution  $\mathcal{F}(\vartheta, n)$  as a function of  $\vartheta$  for the most unstable jet  
235  $n_c$  for the cases with  $\beta = 0.1$  and  $\beta = 100$ . When  $\beta \ll 1$ ,  $\mathcal{F}(\vartheta, n)$  is positive for angles satisfying  
236  $4 \sin^2 \vartheta < 1 + n^2$ . This condition is derived for  $\beta = 0$ , but is also quite accurate for small  $\beta$ , as  
237 shown in Fig. 3(a) (Bakas et al. 2015). The contribution from all angles is small (of order  $\beta^2$ ),  
238 as the positive contribution at small angles is compensated by the negative contribution at larger  
239 angles. For  $\beta \gg 1$ , only waves with phase lines almost parallel to the  $y$  axis ( $|k_y| \approx 0$ ) contribute  
240 significantly to the vorticity fluxes (see Fig. 3). When integrated over all angles, the resulting  
241 vorticity flux feedback is positive and  $O(\beta^{-2})$ . The wave-mean flow dynamics underlying these  
242 contributions at all values of  $\beta$  can be understood by considering the evolution of wave groups in  
243 the sinusoidal flow and were studied in detail by Bakas and Ioannou (2013b).

244 **4. The Ginzburg–Landau (G–L) dynamics governing the nonlinear evolution of the flow-  
245 forming instability**

246 In this section we discuss how the equilibration of the zonal jet instabilities is achieved for  
247 the case just above the critical threshold  $\varepsilon_c$ . As it will be seen, the weak zonal jet equilibria

248 are established through the equilibration of the most unstable eigenfunction with wavenumber  $n_c$   
 249 through a nonlinear feedback which modulates the eddy covariance in order to conserve energy and  
 250 forms jet structures at the second harmonic  $2n_c$ . It is through this energy conservation feedback  
 251 along with the interaction with the  $2n_c$  jet that equilibration is achieved.

252 To derive the asymptotic dynamics that govern the evolution of the jet amplitude we perform  
 253 a multiple-scale perturbation analysis of the nonlinear dynamics near the marginal point. Before  
 254 proceeding with the multiple-scale analysis we present an intuitive argument that suggests the  
 255 appropriate slow time and slow meridional spatial scales.

256 *a. The appropriate slow length scale and slow time scale*

257 For a stochastic excitation with energy input rate  $\varepsilon = \varepsilon_c$ , zonal jets with wavenumber  $n = n_c$  are  
 258 marginally stable. If the energy input rate is slightly supercritical,

$$\varepsilon = \varepsilon_c(1 + \mu^2), \quad (14)$$

259 with  $\mu \ll 1$  a parameter that measures the supercriticality, then zonal jets with wavenumbers  
 260  $|n - n_c| = O(\mu)$  are unstable and grow at a rate of  $O(\mu^2)$ . To see this expand the eigenvalue  
 261 relation (10) near  $\varepsilon_c$ :

$$\sigma = \mu^2 \varepsilon_c f_r + \varepsilon_c \left( \frac{\partial f}{\partial \sigma} \right)_c \sigma + \frac{\varepsilon_c}{2} \left( \frac{\partial^2 f}{\partial n^2} \right)_c (n - n_c)^2 + O[\sigma^2, (n - n_c)^3], \quad (15)$$

262 where the subscript  $c$  denotes that the derivatives are evaluated at the threshold point  $(\sigma, \mu, n) =$   
 263  $(0, 0, n_c)$ .

264 Exactly at the minimum threshold, the function  $f$  has a maximum at  $n = n_c$  ( $(\partial f / \partial n)_c = 0$ )  
 265 and  $(\partial^2 f / \partial n^2)_c < 0$ ) with value  $\varepsilon_c f_r = 1$ , which as seen from (10) implies that  $\sigma = 0$ . Thus the  
 266 approximate eigenvalue relation (15) predicts that the locus of points of marginal stability ( $\sigma = 0$ )

<sup>267</sup> on the  $\varepsilon$ - $n$  plane lie on the parabola:

$$(n - n_c)^2 = \frac{2}{|f''_c|} (\varepsilon/\varepsilon_c - 1) = \frac{2\mu^2}{|f''_c|}, \quad (16)$$

<sup>268</sup> where  $f''_c \stackrel{\text{def}}{=} \partial^2 f / \partial n^2|_c$  and  $\mu$  is the supercriticality parameter.

<sup>269</sup> Using (15) we can estimate the growth rate  $\sigma$  at supercriticality  $\mu$ . We find that jets with  
<sup>270</sup> wavenumber  $n = n_c + \mu v$  grow approximately at rate:

$$\sigma = \mu^2 (1 - c_2 v^2) / c_1, \quad (17)$$

<sup>271</sup> with

$$c_1 \stackrel{\text{def}}{=} 1 - \varepsilon_c \left( \frac{\partial f}{\partial \sigma} \right)_c \quad \text{and} \quad c_2 \stackrel{\text{def}}{=} \frac{\varepsilon_c}{2} |f''_c|. \quad (18)$$

<sup>272</sup> The analytic expressions for  $c_1$  and  $c_2$  are given in (B13) and (B20). Coefficient  $c_1$  is positive for  
<sup>273</sup> stochastic excitations with spectrum (4). From (17), we deduce that for any  $\mu$  only jets with

$$|v| < v_e \stackrel{\text{def}}{=} 1 / \sqrt{c_2}, \quad (19)$$

<sup>274</sup> can become unstable.

<sup>275</sup> Equations (16) and (17) establish the initial assertion: for  $\mu \ll 1$  zonal jets with wavenumbers  
<sup>276</sup>  $|n - n_c| = O(\mu)$  grow at a rate  $\sigma = O(\mu^2)$ .

<sup>277</sup> The validity of the approximate eigenvalue relation (17) as a function of supercriticality  $\mu$  is  
<sup>278</sup> shown in panels (a) and (b) of Fig. 4. By comparing the exact growth rates as given by (10) and  
<sup>279</sup> the growth rates obtained from the approximation (17), we see that the approximate eigenvalue  
<sup>280</sup> dispersion may not be as accurate in three ways: predicting the maximum growth rate, predicting  
<sup>281</sup> the wavenumber at which maximum growth occurs, and predicting the asymmetry of the exact  
<sup>282</sup> growth rates about the maximal wavenumber. These three differences are indicated by the arrows  
<sup>283</sup> in panels (a) and (b) of Fig. 4 and are quantified in panels (c) through (e). Panel (c) compares the  
<sup>284</sup> exact wavenumber of maximum growth  $n_{\max}$  to the critical wavenumber  $n_c$  assumed by approxi-

285 mation (17). We see that  $n_{\max}$  is very close to  $n_c$  up to  $\mu \approx 1$  with the error growing as  $\mu^2$ . This  
 286 is in agreement with the error in (15) being of  $O(\sigma^2)$ . In addition, the exact growth rate  $\sigma(n_c)$  is  
 287 very close to  $\mu^2/c_1$ , as shown in Fig. 4(d) for  $\mu$  up to  $O(1)$ ; the growth rate being overestimated  
 288 by (17) for higher values. Finally, the parabolic approximation (17) to the growth rates predicts  
 289 that the wavenumbers  $\pm v_e$  are marginally stable ( $\sigma(\pm v_e) = 0$ ). Figure 4(e) shows the exact growth  
 290 rates at  $\pm v_e$  at  $\mu = 0.5$ ; these are far from zero for both low and high values of  $\beta$ . The parabolic  
 291 approximation works best for intermediate range  $\beta$  values, i.e., for  $\beta = O(1)$ . To summarize, the  
 292 approximated maximum growth rate  $\mu^2/c_1$  as well as the critical wavenumber  $n_c$  that achieves  
 293 this maximum growth are both good approximations for supercriticalities up to  $\mu = O(1)$ ; the  
 294 parabolic dependence of growth rate for wavenumbers away from  $n_c$  is a good approximation at  
 295  $\mu > 0.1$  only for intermediate values of  $\beta$ . As it will be seen, this has implications on the validity  
 296 of the weakly nonlinear dynamics derived next.

### 297 b. G–L dynamics for weakly supercritical zonal jets

298 Since the excess energy available for flow formation is of order  $\mu^2 \varepsilon_c$ , we expect intuitively  
 299 the mean flow amplitude to be of order  $\mu$ . Therefore, to obtain the dynamics that govern weakly  
 300 supercritical zonal flows, we expand the mean flow  $\bar{u}$  and the covariance  $C$  of the S3T equations (5)  
 301 as:

$$\bar{u} = \mu \bar{u}_1(y, Y, T) + \mu^2 \bar{u}_2(y, Y, T) + O(\mu^3), \quad (20a)$$

$$C = C^e(\mathbf{x}_a - \mathbf{x}_b) + \mu C_1(\mathbf{x}_a, \mathbf{x}_b, Y_a, Y_b, T) + \mu^2 C_2(\mathbf{x}_a, \mathbf{x}_b, Y_a, Y_b, T) + O(\mu^3), \quad (20b)$$

302 Guided by (16) and (17), we have assumed that the zonal jet and its associated covariance evolve  
 303 from the marginal values at the slow time scale  $T \stackrel{\text{def}}{=} \mu^2 t$ , while being modulated at the long  
 304 meridional scale  $Y \stackrel{\text{def}}{=} \mu y$ .

305 Details of the perturbation analysis are given in the Appendix B; here we present the backbone.  
306 We introduce (20) in (5) and gather terms with the same power of  $\mu$ . At leading order  $\mu^0$ , we  
307 recover the homogeneous equilibrium (8). At order  $\mu^1$ , the emergent zonal jet and the covariance  
308 are the modulated S3T eigenfunction:

$$\bar{u}_1 = A(Y, T) e^{in_c y} + \text{c.c.}, \quad (21\text{a})$$

$$C_1 = [A(Y_a, T)G^+(0|\mathbf{x}_a - \mathbf{x}_b) - A(Y_b, T)G^-(0|\mathbf{x}_a - \mathbf{x}_b)] e^{in_c(y_a + y_b)/2} + \text{c.c.}, \quad (21\text{b})$$

309 with  $G_c^\pm$  defined in (A8) and evaluated at  $n = n_c$ .

310 Having determined  $C_1$  we proceed to determine the order  $\mu^2$  correction of the covariance,  $C_2$ .  
311 This step of the calculation is facilitated if we disregard the dependence on the slow spatial scale  $Y$   
312 in the amplitude  $A$ , as well as that in  $C_1$  and  $C_2$ . Parker and Krommes (2014) showed that the  
313 nonlinear term of the asymptotic dynamics responsible for the equilibration of the amplitude  $A$   
314 can be obtained using this simplification, while the contribution to the asymptotic dynamics from  
315 the slow varying latitude  $Y$  is the addition of a diffusion term with the diffusion coefficient  $c_2$   
316 in (18). At order  $\mu^2$  a zonal jet with wavenumber  $2n_c$  emerges:

$$\bar{u}_2 = \alpha_2 A(T)^2 e^{2in_c y} + \text{c.c.}, \quad (22\text{a})$$

317 where  $\alpha_2$  is given in (B7) and for the forcing considered is negative ( $\alpha_2 < 0$ ). The associated  
318 covariance at order  $\mu^2$ ,

$$C_2 = C^e(\mathbf{x}_a - \mathbf{x}_b) + C_{20}(\mathbf{x}_a - \mathbf{x}_b) + C_{22}(\mathbf{x}_a - \mathbf{x}_b) e^{2in_c(y_a + y_b)/2} + \text{c.c.}. \quad (22\text{b})$$

319 consists of the homogeneous part,  $C^e + C_{20}$ , and also an inhomogeneous contribution at wavenum-  
320 ber  $2n_c$ . (Note that, as implied by (14), the forcing covariance  $Q$  appears both at order  $\mu^0$  and at  
321 order  $\mu^2$ .)

322 The homogeneous covariance contribution,  $C^e + C_{20}$ , is required at order  $\mu^2$  so that the energy  
 323 conservation (7) is satisfied. To show this note that as the instability develops on a slow time scale,  
 324 the total energy density has already assumed (over an order one time scale) its steady state value  
 325  $\varepsilon/2$  (see (7)) and therefore, the mean flow energy growth *must* be accompanied by a decrease in  
 326 the eddy energy. This decrease is facilitated by a concomitant change of the eddy covariance at  
 327 order  $\mu^2$ . Specifically, by introducing perturbation expansion (20) in (7) at steady state, we obtain  
 328 at leading order,  $\mu^0$ , the trivial balance:

$$-\int_{\infty} d^2 \mathbf{x} \frac{1}{4} [(\Delta_a^{-1} + \Delta_b^{-1}) C^e]_{a=b} = \frac{\varepsilon_c}{2}. \quad (23)$$

329 At order  $\mu^1$  the eddy covariance does not contribute to the energy since  $C_1$  is harmonic in  $y$  and  
 330 integrates to zero:

$$\int_{\infty} d^2 \mathbf{x} \frac{1}{4} [(\Delta_a^{-1} + \Delta_b^{-1}) C_1]_{a=b} = 0. \quad (24)$$

331 At order  $\mu^2$  we use (i) (23) and (ii) that the inhomogeneous component  $C_{22} e^{2i n_c (y_a + y_b)/2}$  is har-  
 332 monic and integrates to zero, to obtain:

$$\int_{\infty} d^2 \mathbf{x} \frac{1}{4} [(\Delta_a^{-1} + \Delta_b^{-1}) C_{20}]_{a=b} = \int_{\infty} d^2 \mathbf{x} \frac{1}{2} \bar{u}_1^2. \quad (25)$$

333 Thus the homogeneous deviation from the equilibrium covariance must produce a perturbation  
 334 energy *defect* to counter balance the energy growth of the mean flow. We refer to  $C_{20}$  as the *eddy*  
 335 *energy correction term*. However, we note that the correction to the homogeneous part of the  
 336 covariance does not only change the mean eddy energy but also other eddy characteristics, such as  
 337 the mean eddy anisotropy, that also might play a role in the equilibration process.

338 At order  $\mu^3$  secular terms appear which, if suppressed, yield an asymptotic perturbation expan-  
 339 sion up to time  $O(1/\mu^2)$ . Suppression of these secular terms requires that the amplitude  $A$  of the  
 340 most unstable jet with wavenumber  $n_c$  satisfies:

$$c_1 \partial_T A = A - c_3 A |A|^2. \quad (26)$$

<sup>341</sup> If we now allow the amplitude to also evolve with the slow scale,  $Y$ , and add the diffusion term  
<sup>342</sup>  $c_2 \partial_Y^2 A$  on the right-hand-side of (26), we obtain the real Ginzburg–Landau (G–L) equation:

$$c_1 \partial_T A = A + c_2 \partial_Y^2 A - c_3 A |A|^2 . \quad (27)$$

<sup>343</sup> For forcing with spectrum (4) all three coefficients  $c_1$ ,  $c_2$ , and  $c_3$  are real and positive. The coeffi-  
<sup>344</sup> cients  $c_1$  and  $c_2$ , are the coefficients in the Taylor expansion (15) and are given in (18).

<sup>345</sup> The G–L equation (27) has a steady solution  $A = 0$ . This solution is linearly unstable to modal  
<sup>346</sup> perturbations  $e^{ivY+\sigma T}$ , with growth rate  $\mu^2(1-v^2c_2)/c_1$ ; the most unstable mode occurs at  $v =$   
<sup>347</sup> 0. This is the flow-forming SSD instability of the homogeneous equilibrium state in the G–L  
<sup>348</sup> framework (cf. (17)). The G–L equation has also the nonlinear harmonic equilibria

$$A(Y) = R_0(v) e^{i(vY+\varphi)} \text{ with } R_0(v) = \sqrt{(1-v^2c_2)/c_3} , \quad (28)$$

<sup>349</sup> and  $\varphi$  an undetermined phase that reflects the translational invariance of the system in  $y$ . These  
<sup>350</sup> equilibria are the possible finite-amplitude jets that emerge at low supercriticality. However, as  
<sup>351</sup> will be shown in the next section, some of these equilibria are susceptible to a secondary SSD  
<sup>352</sup> instability and evolve through jet merging or jet branching to the subset of the stable attracting  
<sup>353</sup> states.

<sup>354</sup> The G–L equation obeys potential dynamics and thus the system always ends up in a stationary  
<sup>355</sup> state which is a local minimum of the potential (Cross and Greenside 2009). The  $v = 0$  jet is the  
<sup>356</sup> state that corresponds to the global minimum of the potential and it has amplitude

$$R_0(0) = 1/\sqrt{c_3} . \quad (29)$$

357 **5. Comparison of the predictions of G–L dynamics with S3T dynamics for the equilibrated**  
 358 **jets**

359 In this section we test the validity of the weakly nonlinear G–L dynamics by comparing its  
 360 predictions for the amplitude of the equilibrated jets with fully nonlinear S3T dynamics. We  
 361 consider the S3T dynamical system (5) in a doubly periodic domain  $2\pi L_* \times 2\pi L_*$  with a  $128^2$   
 362 grid-resolution and  $L_* = 1$ , as well as the G–L dynamics with periodic boundary conditions for  
 363 the amplitude of the jet,  $A$ , on the same domain. We approximate the delta function in the ring  
 364 forcing (4) with

$$\delta(k_* - k_{f*}) \mapsto \frac{e^{-(k_* - k_{f*})^2 / (2\delta_{f*}^2)}}{\sqrt{2\pi}\delta_{f*}}, \quad (30)$$

365 with  $k_{x*}L_*$ ,  $k_{y*}L_*$  assuming integer values. (The asterisks denote dimensional values, as in,  
 366 e.g., (1).) Forcing (30) injects energy in a narrow ring in wavenumber space with radius  $k_{f*}L_* = 10$   
 367 and width  $\delta_{f*}L_* = 1.5$ . We note that even though (30) is a good approximation of the delta-ring  
 368 forcing (4)), small quantitative differences are to be expected. For example, the critical energy in-  
 369 put rates for jet emergence obtained from the discrete finite ring excitation differ by as much as 4%  
 370 from the corresponding values obtained from the delta-ring forcing (4). Since the equilibrated jet  
 371 amplitudes are of order  $\mu \ll 1$ , we use the exact values for the critical energy input rates obtained  
 372 for the discrete finite ring excitation.

373 We also consider  $r_* = 0.1$  and vary  $\beta_*$  as well as the energy input rate  $\varepsilon_*$  that is the bifurcation  
 374 parameter. The eigenvalue relation for the flow-forming instability can be readily obtained by sub-  
 375 stituting the integrals in (10) with sums over the allowed wavenumbers. However, the comparison  
 376 with the predictions of the G–L dynamics with periodic boundary conditions in the meridional  
 377 is more tricky. Due to the periodic boundary conditions in the jet amplitude, a harmonic mean  
 378 flow  $A(Y, T) = e^{ivY}$  with wavenumber  $v$  corresponds to a mean flow within our domain *only* if its

dimensional wavenumber  $n_* = (\mu v + n_c)k_{f*}$  is an integer. Therefore, we carefully pick  $\beta_*$  so that the marginal wavenumber  $n_c k_{f*}$  always assumes an integer value; for  $k_{f*} = 10/L_*$  this leaves us with nine possible values for  $\beta_*$  covering the range  $3 \times 10^{-1} < \beta_* < 2 \times 10^3$ . The lowest and highest marginal  $\beta_*$ -values yield marginal jets at the lowest and highest allowed wavenumber possible within our domain;  $1/L_*$  and  $k_{f*} - 1/L_*$  respectively. We excluded these values for  $\beta_*$ , since they do not allow us to study the finite amplitude stability of side-band jets (i.e., jets at larger or smaller scale compared to the scale of  $n_{c*}$ ). Therefore, in our comparisons we use only the remaining seven values of  $\beta_*$ , which are shown in Table 1.

We calculate the finite amplitude equilibrated jets from the nonlinear S3T dynamical system (5) using a Newton's method with the initial guess provided by (29).<sup>2</sup> All jet equilibria we compute in this section are hydrodynamically stable. At small supercriticalities the jet amplitude is small and the linear operator is dominated by dissipation. Thus, all instabilities we discuss here are “SSD instabilities” (see the discussion in §3 of section 1).

### a. Equilibration of the most unstable jet, $n_c$

Consider first the most unstable jet perturbation with wavenumber  $n_c$ . Figure 5 shows the Fourier amplitude of the equilibrated jet dominated by wavenumber  $n_c$  for four values of  $\beta$ . We see that for  $\beta \lesssim 12$ , the amplitude is given, to a very good approximation, by (29) for supercriticality up to  $\mu \approx 0.2$  (see panels (a)-(b)). For larger supercriticality, the amplitude of the equilibrated jet is not well captured by (29); the jet amplitude is overestimated for  $\beta \lesssim 12$  while it is underestimated for  $\beta \gtrsim 12$ . We note here, that S3T equilibria with dominant wavenumber  $n_c$  (as predicted by the G–L dynamics) exist at even larger supercriticalities but these were found to be S3T unstable.

---

<sup>2</sup>For details regarding Newton's algorithm for system (5) the reader is referred to the Appendix I in the thesis of Constantinou (2015).

400 Surprisingly, for  $\beta \gtrapprox 20$  there exist multiple equilibria for the same supercriticality  $\mu$  (see pan-  
 401 ells (c)-(d) of Fig. 5). Specifically, there exists a branch of stable equilibria apart from the jets  
 402 connected to the homogeneous equilibrium (cf. triangles in Fig. 5(c)-(d) versus the circles). For  
 403  $\mu \gtrapprox 0.2$ , the lower branch equilibria, predicted by the G–L dynamics, do not exist; an infinitesimal  
 404 harmonic jet perturbation with wavenumber  $n_c$  ends up in the upper branch. Equally interesting is  
 405 the fact that the upper branch extends to subcritical values of the energy input rate with respect to  
 406 the flow-forming instability of the homogeneous state, i.e. for  $\varepsilon < \varepsilon_c$ . This is shown in Fig. 6(a)  
 407 for  $\beta_{58}$  and similar subcritical jet equilibria were found for  $\beta_{24}$  and  $\beta_{192}$  (not shown). Thus, apart  
 408 from the linear instability forming jets that has been extensively studied in the literature, there  
 409 is a nonlinear instability for jet formation the details of which will be discussed in section 6b.  
 410 Since both the upper and the lower branch exist for a limited range of energy input rates, there is  
 411 a hysteresis loop shown in Fig. 6(a), with the dynamics landing on the upper or the lower branch  
 412 of jet equilibria as  $\varepsilon$  is varied. The two stable branches are connected with a branch of unstable  
 413 equilibria (open circles) that were also found using Newton’s method.

414 The jets on the lower and the upper stable branch are qualitatively different. Panels (b)-(e) of  
 415 Fig. 6 compare the jet structure and spectra of two such equilibria in the case of  $\beta_{58}$  and  $\mu = 0.05$ .  
 416 While the lower branch jet consists mainly of  $n_c$  and its double harmonic,  $2n_c$ , with a much weaker  
 417 Fourier amplitude in qualitative agreement with the G–L prediction of  $\bar{u}_2 \approx O(\mu^2 A^2)$  (c.f. (22a)),  
 418 the upper branch jet is stronger by two orders of magnitude, it contains more harmonics and the  
 419 Fourier amplitude of the double harmonic  $2n_c$  is about half the amplitude of the leading harmonic  
 420  $n_c$ . As will be elaborated in section 6b, it is the interaction of the two jets with wavenumbers  $n_c$   
 421 and  $2n_c$  that supports the upper branch equilibria.

<sup>422</sup> b. Equilibration of the side-band jets,  $n_c \pm 1/(k_{f*}L_*)$

<sup>423</sup> We now consider the jet equilibria that emerge from the equilibration of jet perturbations with  
<sup>424</sup> wavenumbers close to  $n_c$ . While for an infinite domain there is a dense set of unstable jet per-  
<sup>425</sup> turbations with wavenumbers  $\mu v$  close to  $n_c$  (cf. (19)), for the doubly periodic box the first side  
<sup>426</sup> band jet instabilities have dimensional wavenumbers  $n_*^\pm = n_c k_{f*} \pm 1/L_*$ , or  $v^\pm = \pm 1/(k_{f*}L_*\mu)$ .  
<sup>427</sup> Introducing  $v^\pm$  in (19), we obtain that the parabolic approximation predicts that the homogeneous  
<sup>428</sup> equilibrium becomes unstable to jet perturbations with wavenumber  $v^\pm$  when  $\mu_{\text{GL}} > \sqrt{c_2}/(k_{f*}L_*)$ .  
<sup>429</sup> However, as shown in Fig. 4(d), the parabolic approximation is not accurate especially at low and  
<sup>430</sup> large values of  $\beta$ . For example for  $\beta_1$ ,  $\mu_{\text{GL}} = 0.4293$ , while the exact dispersion relation predicts  
<sup>431</sup> that jets with  $v_+$  and  $v_-$  are rendered neutral at  $\mu_{\text{ex}^+} = 0.2140$  and  $\mu_{\text{ex}^-} = 0.7953$  respectively.  
<sup>432</sup> We therefore expect significant deviations from (28) for the amplitude of the equilibrated jets.

<sup>433</sup> Figure 7 shows the equilibrated amplitude of the side band jet perturbations with  $v^\pm$  as a func-  
<sup>434</sup> tion of supercriticality for four values of  $\beta$ . While the functional dependence of the equilibrated  
<sup>435</sup> amplitude on  $\mu$  is qualitatively captured by (28) (dashed lines), there are significant quantitative  
<sup>436</sup> differences especially for  $\beta_1$  and  $\beta_{192}$ . Since these quantitative differences are due to the failure of  
<sup>437</sup> the parabolic approximation, a way to rectify them is to use an equivalent

$$c_2^{\text{ex}\pm} \stackrel{\text{def}}{=} (k_{f*}L_*\mu_{\text{ex}\pm})^2, \quad (31)$$

<sup>438</sup> based on the supercriticality  $\mu_{\text{ex}}^\pm$  obtained from the exact dispersion relation (10). The solid curves  
<sup>439</sup> show the predicted amplitude using  $c_2^{\text{ex}\pm}$ . We observe that for all values of  $\beta$  the amplitude of  
<sup>440</sup> the jets close to the bifurcation point is accurately predicted and for the intermediate value of  $\beta_6$   
<sup>441</sup> for which the exact dispersion is the closest to the parabolic profile, the agreement holds away  
<sup>442</sup> from the bifurcation point as well. Finally, note that for large  $\beta$  shown in Fig. 7(c) the additional  
<sup>443</sup> upper branch of equilibria is found and has the same characteristics as the upper branch of  $n_c$

equilibria. That is, the equilibrated jets have a larger amplitude and the Fourier amplitude of the double harmonic (in this case it is the  $2(n_c + 1/\mu k_{f*} L_*)$  harmonic) is much larger compared to the G-L branch.

Finally, we stress that the results in this section regarding the existence of the upper branch equilibria as well as the accuracy of the G-L dynamics for the lower branch equilibria are not quirks of the particular isotropic forcing structure in (4) but rather similar qualitative behavior is found for forcing with anisotropic spectrum. Discussion regarding the effects of the structure of the forcing is found in Appendix C.

## 6. The physical processes underlying the equilibration of the SSD instability of the homogeneous state

One of the main objectives of this paper is to study the processes that control the halting of the flow-forming instability both for the low branch equilibria, which are governed by the G-L dynamics, and for the upper branch equilibria (cf. Figs. 5 and 6).

### a. Equilibration processes for the lower branch

For G-L dynamics, the equilibration of the instability for the most unstable jet perturbation with wavenumber  $n_c$  as well as for sideband jets (i.e., jets with scales close to  $n_c$ ) is controlled by coefficient  $c_3$  in (27). We start with a discussion on how  $c_3$ , and consequently of the equilibration amplitude  $R_0(0)$ , depends on  $\beta$ ; Fig. 8(a) shows the amplitude of the most unstable jet,  $R_0(0)$ , as a function of  $\beta$ . For  $\beta \gg 1$  the emerging jets have large scales ( $n_c \ll 1$ ) and equilibrate with amplitude that increases as  $R_0 \sim \beta^{1/3}$ . For  $\beta \ll 1$ , the emerging jets have small scales ( $n_c \approx 1$ ) and their amplitude scales as  $R_0 \sim \beta^{2/3}$ . The scaling of  $R_0$  for  $\beta \gg 1$  is found to be robust feature independent of the spectral properties of the forcing (cf. Fig. 8 and Fig. 17). On the other hand

466 for  $\beta \gg 1$  the amplitude  $R_0$  depends crucially on the forcing structure; see Appendix C. However,  
467 the regime  $\beta \ll 1$  is uninteresting anyway since the anisotropy in the dynamics in (1) becomes  
468 vanishingly small and no zonal jets emerge.

469 The dependence of the amplitude  $R_0(0)$  on  $\beta$  can be understood by considering the contribution  
470 of the various wave components to  $c_3$ , in a similar manner as we did for  $f_r$  in (13). Thus, we write:

$$c_3 = \int_0^{\pi/2} \mathcal{F}_{\text{NL}}(\vartheta) d\vartheta , \quad (32)$$

471 where  $\mathcal{F}_{\text{NL}}$  is the contribution to  $c_3$  from the four waves with wavevectors  $\mathbf{k} = (\pm \cos \vartheta, \pm \sin \vartheta)$ .  
472 Figure 3 shows the contributions  $\mathcal{F}_{\text{NL}}(\vartheta)$  for two values of  $\beta$ .

473 For  $\beta \ll 1$ , all wave orientations contribute positively to  $c_3$ . As a result, the up-gradient con-  
474 tributions to the vorticity flux feedback  $\mathcal{F}$  at small  $\vartheta$  are counteracted by  $\mathcal{F}_{\text{NL}}$ , while the down-  
475 gradient contributions to  $\mathcal{F}$  at higher  $\vartheta$  are enhanced by  $\mathcal{F}_{\text{NL}}$ . This leads to a rapid quenching of  
476 the instability and thus to a weak finite amplitude jet.

477 For large  $\beta$ ,  $\mathcal{F}_{\text{NL}}$  has roughly the same dipole structure centered about an angle  $\vartheta_0$  as the  
478 vorticity flux feedback  $\mathcal{F}$ . Therefore, only waves with angles close to  $\vartheta_0$  contribute appreciably  
479 to  $c_3$ . Waves with angles  $|\vartheta| < \vartheta_0$  give positive contributions to  $c_3$ , while waves with angles  
480  $|\vartheta| > \vartheta_0$  give negative contributions to  $c_3$ . As a result, both the up-gradient and the down-gradient  
481 contributions to  $\mathcal{F}$  are almost equally reduced and the instability is only slowly hindered and is  
482 allowed to drive jets with a much larger amplitude compared to  $\beta \ll 1$ . To understand the power  
483 law increase of  $R(0)$  with  $\beta$ , note that as  $\beta$  increases: (i) the heights of the dipole peaks grow  
484 linearly with  $\beta$ , (ii) the widths of the dipole peaks decrease as  $\beta^{-2/3}$ , and (iii) the structure of  
485 dipole becomes more symmetric about  $\vartheta_0$ . Figure 9(a) demonstrates points (i)-(iii). Thus, each  
486 of the positive and the negative contribution to  $c_3$  scale as  $\beta \times \beta^{-2/3} = \beta^{1/3}$  and their difference

<sup>487</sup> scales with the derivative, i.e., as  $d\beta^{1/3}/d\beta \propto \beta^{-2/3}$  leading to the increase of  $R(0)$  with  $\beta$  as  
<sup>488</sup>  $\beta^{1/3}$ .

<sup>489</sup> Next we investigate how each of the forced waves contribute in sustaining the equilibrated state  
<sup>490</sup> of the most unstable jet ( $v = 0$ ) with amplitude  $R_0(0)$  by decomposing the portion of the vorticity  
<sup>491</sup> flux exceeding dissipation which is the sum of  $f_r$  and  $-c_3R_0(0)^2$ , into contributions from various  
<sup>492</sup> wave angles:

$$f_r - c_3R_0(0)^2 = \int_0^{\pi/2} [\mathcal{F}(\vartheta) - R_0^2 \mathcal{F}_{NL}(\vartheta)] d\vartheta. \quad (33)$$

<sup>493</sup> Figure 9(b) shows these contributions for three values of  $\beta$ . For small values of  $\beta$  waves with  
<sup>494</sup> angles  $|\vartheta| < \pi/4$  that drive the instability through their up-gradient contribution also support the  
<sup>495</sup> equilibrated jet. However, for  $\beta \gg 1$  this picture is reversed. The instability is driven by waves  
<sup>496</sup> with  $|\vartheta| < \vartheta_0$  (mainly from waves with  $|\vartheta| \approx 0$ ) and is hindered by waves with angles  $|\vartheta| > \vartheta_0$ ,  
<sup>497</sup> while the equilibrated jet is supported through the up-gradient fluxes of waves with angles  $|\vartheta| > \vartheta_0$ .  
<sup>498</sup> The reason is the amplitude  $R_0(0)$  is so large that the sign of the integrand in (33) is reversed.  
<sup>499</sup> Further investigation of the eddy–mean flow interactions leading to this peculiar feedback is out  
<sup>500</sup> of the scope of the current work and will be reported in a future study.

<sup>501</sup> Further insight into the equilibration dynamics is gained by noting that the coefficient  $c_3$  can be  
<sup>502</sup> written as the sum of two separate contributions:

$$c_3 = c_3^{ec} + c_3^{1,2}, \quad (34)$$

<sup>503</sup> which represent different physical processes (details on the decomposition can be found in Ap-  
<sup>504</sup> pendix B). These contributions correspond to the two  $O(\mu^3)$  possible interactions between the  
<sup>505</sup> perturbed components of the mean flow  $\mu \bar{u}_1$  and  $\mu^2 \bar{u}_2$  with the covariance corrections  $\mu C_{11}$ ,  $\mu^2 C_{20}$ ,  
<sup>506</sup>  $\mu^2 C_{22}$ .

507 Coefficient

$$c_3^{ec} \propto -f(0 | \bar{u}_1, C_{20}) , \quad (35)$$

508 is proportional to the mean vorticity flux feedback from the interaction of  $\mu\bar{u}_1$  with the homo-  
509 geneous covariance correction  $\mu^2C_{20}$  to the equilibrium  $C^e$ . It measures the compensation in the  
510 vorticity flux as perturbations lose energy to the mean flow.

511 Coefficient

$$c_3^{1,2} \propto -f(0 | \bar{u}_1, C_{22} e^{2in_c(y_a+y_b)/2} + \text{c.c.}) - f(0 | \bar{u}_2, C_1) , \quad (36)$$

512 measures the mean vorticity flux feedbacks from the interaction of  $\mu\bar{u}_1$  and  $\mu^2\bar{u}_2$  with the inho-  
513 mogeneous covariance corrections  $\mu C_1$  and  $\mu^2 C_{22} e^{2in_c(y_a+y_b)/2}$  to the equilibrium  $C^e$ . The exact  
514 form of the coefficients is given in (B16) and (B18) respectively.

515 Figure 8(b) shows the contribution of the two processes in  $c_3$  as a function of  $\beta$ . We observe that  
516 the main contribution to the coefficient  $c_3$  comes from  $c_3^{ec}$  for most values of  $\beta$ . Only for  $\beta \ll 1$   
517 is there a contribution from  $c_3^{1,2}$  at the same order.<sup>3</sup> The same results also hold for the case of the  
518 anisotropic forcing; see Fig. 17. Therefore, we conclude that for most values of  $\beta$ , the mean flow  
519 is stabilized by the change in the homogeneous part of the covariance due to conservation of the  
520 total energy that leads to a concomitant reduction of the up-gradient fluxes. For  $\beta \ll 1$  there is  
521 no change in the eddy–mean flow dynamical processes involved, while for  $\beta \gg 1$  the equilibrated  
522 flow is supported by the up-gradient fluxes of the eddies that were initially hindering its formation.

523 *b. Equilibration processes for the upper-branch jets*

524 We have seen in the discussion surrounding Fig. 6, that the  $2n_c$ -components of the upper branch  
525 equilibria are much stronger than the corresponding  $2n_c$ -components of the lower branch jets.  
526 Therefore, we expect the interaction between the jet components with wavenumbers  $n_c$  and  $2n_c$

---

<sup>3</sup>Further analysis on the relative contributions of the forced eddies on the for the two distinct processes can be found in Appendix B.

527 to play an important role in the equilibration of the upper-branch jets. This is not at all the case  
 528 for the lower branch G–L equilibria for which this interaction quantified by  $c_3^{1,2}$  is sub-dominant  
 529 compared to the energy correction term  $c_3^{ec}$ .

530 To investigate the interaction between the jet components with wavenumbers  $n_c$  and  $2n_c$ , we  
 531 impose a mean flow with power only at those Fourier components:

$$\bar{u} = \hat{\bar{u}}_1 e^{in_c y} - \hat{\bar{u}}_2 e^{2in_c y} + \text{c.c.} . \quad (37)$$

532 At low supercriticality there is a phase difference of  $180^\circ$  between the two components (see (22a)  
 533 and the fact that  $\alpha_2 < 0$ ). Therefore, we impose the same phase difference in (37). We then  
 534 compute the vorticity fluxes which are induced by the mean flow (37) by employing the adiabatic  
 535 approximation, i.e., by assuming that the mean flow evolves slow enough that it remains in equi-  
 536 librium with the eddy covariance and thus  $\partial_t C \approx 0$ . Such an adiabatic approximation is exact for  
 537 the fixed points of the S3T dynamics but it has also been proven adequate in qualitatively illumi-  
 538 nating the eddy–mean flow dynamics away from the homogeneous or inhomogeneous equilibria  
 539 (Farrell and Ioannou 2003, 2007; Bakas and Ioannou 2013b; Bakas et al. 2015). With the adiabatic  
 540 approximation, the Lyapunov equation (5b) simplifies to:

$$-\mathcal{L}C + \mathcal{N}(\hat{\bar{u}}_1 e^{in_c y} - \hat{\bar{u}}_2 e^{2in_c y} + \text{c.c.}, C) + \varepsilon Q = 0 . \quad (38)$$

541 We solve (38) for  $C$ , we compute the vorticity fluxes and decompose them into their Fourier  
 542 components:

$$\underbrace{\overline{v' \zeta'}}_{=\mathcal{R}(C)} = \sum_m \hat{f}_{mn_c}(\hat{\bar{u}}_1, \hat{\bar{u}}_2) e^{imn_c y} + \text{c.c.} , \quad (39)$$

543 with  $m$  positive integer. Then, from the mean flow equation (5a), we obtain that the mean flow  
 544 components satisfy:

$$\frac{d\hat{u}_1}{dt} = \hat{f}_{n_c}(\hat{u}_1, \hat{u}_2) - \hat{u}_1 , \quad (40a)$$

$$\frac{d\hat{u}_2}{dt} = \hat{f}_{2n_c}(\hat{u}_1, \hat{u}_2) - \hat{u}_2 . \quad (40b)$$

545 Figure 10 shows the mean flow growth rates (e.g.,  $(1/\hat{u}_1)d\hat{u}_1/dt$ ) as a function of the components  
 546  $\hat{u}_1$  and  $\hat{u}_2$  of the imposed mean flow. We see that for an infinitesimal mean flow (lower left corner  
 547 of the two panes; noted as region G–L), the growth of  $\hat{u}_1$  resulting from the linear instability and  
 548 the growth of  $\hat{u}_2$  resulting from the second order self-interaction of the unstable mode (c.f. (22a))  
 549 lead to an increase of both  $\hat{u}_1$  and  $\hat{u}_2$ . The flow, thus, equilibrates at the point of intersection of the  
 550 zero contours for both mean flow tendencies (thick white curves). This is the lower branch G–L  
 551 equilibrium that is shown by the open circle and was discussed in the previous section.

552 There exist, however, two additional points of intersection, both of which are accessible to the  
 553 flow through paths in the  $\hat{u}_1$ – $\hat{u}_2$  parameter space. If we start with a strong  $\hat{u}_1 \gtrapprox 0.14$  component  
 554 from point A in the figure, the large positive growth rate  $(1/\hat{u}_2)d\hat{u}_2/dt$  will lead to a rapid increase  
 555 of  $\hat{u}_2$ , while the slightly negative tendency  $(1/\hat{u}_1)d\hat{u}_1/dt$  will gradually weaken  $\hat{u}_1$  so that  $\hat{u}_2$   
 556 and  $\hat{u}_1$  will move towards the right point of intersection. We perform an integration of the S3T  
 557 dynamical system (5) with initial conditions starting from point A. The path of the dynamical  
 558 system in the  $\hat{u}_1$ – $\hat{u}_2$  parameter space that is shown by the dotted line, confirms the qualitative  
 559 picture obtained via the mean flow growth rates with the rapid increase of  $\hat{u}_2$  and the eventual  
 560 equilibration at the right point of intersection shown by the filled triangle. Similarly, if we start  
 561 with a strong  $\hat{u}_2 \gtrapprox 0.2$  component from point B, the strong growth  $(1/\hat{u}_1)d\hat{u}_1/dt$  and the weak  
 562 negative tendency  $(1/\hat{u}_2)d\hat{u}_2/dt$  lead again to the equilibration of the flow through the path shown  
 563 in Fig. 10. The growth rates close to the other point of intersection shown by the open circle reveals

564 that this corresponds to an unstable equilibrium and this is also confirmed through integrations of  
 565 the S3T system (5). These two points therefore correspond to the stable and unstable equilibria of  
 566 the upper branch that are shown in Fig. 6.

567 The qualitative agreement between the approximate dynamics of (40) and the nonlinear S3T  
 568 dynamics reveal that it could be a useful tool for exploring the phase space of the S3T system.  
 569 For example, the bifurcation structure of Fig. 6 could be obtained by plotting the adiabatic growth  
 570 rates. Figure 11 shows the curves of zero tendencies for various values of the supercriticality.  
 571 For low subcritical values  $\varepsilon/\varepsilon_c < 0.89$  (panel (a)), there is no point of intersection, therefore  
 572 only the homogeneous equilibrium exists. For  $0.89 \leq \varepsilon/\varepsilon_c < 1$  (panel b), there are two points of  
 573 intersection revealing the existence of the stable and the unstable upper branch equilibria, while  
 574 for  $1 \leq \varepsilon/\varepsilon_c$  (panel (c)) there is the additional lower branch point. Finally, for highly supercritical  
 575 values (panel (d)) there is only one point of intersection revealing the existence of the stable upper  
 576 branch equilibrium.

577 To shed light into the dynamics underlying these new equilibration paths that lead to the upper-  
 578 branch equilibria, we decompose the covariance as a Fourier sum over the inhomogeneous com-  
 579 ponents

$$C = \sum_{m=0}^4 \hat{C}_m(\mathbf{x}_a - \mathbf{x}_b) e^{imn_c(y_a + y_b)/2}. \quad (41)$$

580 The sum is over five components. The reason is that first of all the flux feedback on  $\hat{u}_1$  and  $\hat{u}_2$  is  
 581 generated by the  $n_c$  and  $2n_c$  components of the covariance. Inspection of the nonlinear term in (38),  
 582 reveals that only the homogeneous component  $\hat{C}_0$  as well as the covariance components at  $n_c$ ,  $2n_c$ ,  
 583  $3n_c$  and  $4n_c$  can interact with the mean flow (37) to yield these two covariance components. We

584 then decompose the vorticity fluxes as:

$$\hat{f}_{n_c}(\hat{\bar{u}}_1, \hat{\bar{u}}_2) = f_{1,0} + f_{1,2} + f_{2,3}, \quad (42a)$$

$$\hat{f}_{2n_c}(\hat{\bar{u}}_1, \hat{\bar{u}}_2) = f_{2,0} + f_{1,1} + f_{1,3} + f_{2,4}. \quad (42b)$$

585 Each of the terms on the right-hand-sides of (42) represents the different interactions among the  
 586 mean flow components  $\hat{\bar{u}}_1, \hat{\bar{u}}_2$  with the covariance components  $\hat{\bar{C}}_0, \hat{\bar{C}}_1, \hat{\bar{C}}_2, \hat{\bar{C}}_3$  and  $\hat{\bar{C}}_4$ . The first  
 587 term in (42a) is proportional to the vorticity flux feedback from the interaction of  $\hat{\bar{u}}_1$  with the  
 588 homogeneous covariance component  $\hat{\bar{C}}_0$ :

$$f_{1,0} \propto f(0 | \hat{\bar{u}}_1 e^{in_c y}, \hat{\bar{C}}_0). \quad (43)$$

589 For low supercriticality,

$$f_{1,0} - \hat{\bar{u}}_1 \approx A(1 - c_3^{ec}|A|^2). \quad (44)$$

590 This means that  $f_{1,0}$  contains both the destabilizing feedback which drives the linear instability,  
 591 and the stabilizing feedback at finite amplitude that results from the energy correction. The terms  
 592  $f_{1,2}$  and  $f_{2,3}$  in (42a) describe the feedback of the nonlinear interaction between  $\hat{\bar{u}}_1$  and  $\hat{\bar{u}}_2$  on  $\hat{\bar{u}}_1$ :

$$f_{1,2} \propto f(0 | \hat{\bar{u}}_1^* e^{-in_c y}, \hat{\bar{C}}_2 e^{2in_c(y_a+y_b)/2}) + f(0 | \hat{\bar{u}}_2 e^{2in_c y}, \hat{\bar{C}}_1^* e^{-in_c(y_a+y_b)/2}), \quad (45)$$

$$f_{2,3} \propto f(0 | \hat{\bar{u}}_2^* e^{-2in_c y}, \hat{\bar{C}}_3 e^{3in_c(y_a+y_b)/2}). \quad (46)$$

593 For low supercriticality

$$f_{1,2} \approx -c_3^{1,2} A|A|^2, \quad (47)$$

594 while  $f_{2,3}$  is of higher order in  $\mu$ . Similarly, the second term on the right-hand-side of (42b)  
 595 is proportional to the vorticity flux feedback from the interaction of  $\hat{\bar{u}}_2$  with the homogeneous  
 596 covariance  $\hat{\bar{C}}_0$ :

$$f_{2,0} \propto f(0 | \hat{\bar{u}}_2 e^{2in_c y}, \hat{\bar{C}}_0). \quad (48)$$

597 For low supercriticality, the flux feedback above is positive but does not overcome friction, i.e.,  
 598  $0 < f_{2,0} < \hat{u}_2$ . Therefore, the homogeneous equilibrium is linearly stable with respect to jet per-  
 599 turbations with wavenumber  $2n_c$  (as expected). The terms  $f_{1,1}$ ,  $f_{1,3}$  and  $f_{2,4}$  in (42b) describe the  
 600 feedback of the nonlinear interaction between  $\hat{u}_1$  and  $\hat{u}_2$  on  $\hat{u}_2$ :

$$f_{1,1} \propto f\left(0 \mid \hat{u}_1 e^{in_c y}, \hat{\bar{C}}_1 e^{in_c(y_a+y_b)/2}\right), \quad (49)$$

$$f_{1,3} \propto f\left(0 \mid \hat{u}_1^* e^{-in_c y}, \hat{\bar{C}}_3 e^{3in_c(y_a+y_b)/2}\right) \quad (50)$$

$$f_{2,4} \propto f\left(0 \mid \hat{u}_1^* e^{-2in_c y}, \hat{\bar{C}}_4 e^{4in_c(y_a+y_b)/2}\right). \quad (51)$$

601 For low supercriticality,  $f_{1,1}$  drives the  $\hat{u}_2$  component of the flow with an amplitude proportional  
 602 to  $\hat{u}_1^2$  and, therefore,  $\hat{u}_2$  equilibrates at amplitude (22a), while  $f_{1,3}$  and  $f_{2,4}$  are of higher order.  
 603 Panels (c)-(i) of Fig. 10 show the contribution of the various terms to the flux feedbacks  $\hat{f}_{n_c}$  and  
 604  $\hat{f}_{2n_c}$  respectively. In the G–L region the fluxes are determined by  $f_{0,1}$ ,  $f_{0,2}$  and  $f_{1,1}$ . However,  
 605 the “tongue” of positive tendency  $(1/\hat{u}_1)d\hat{u}_1/dt$  in Fig. 10(a) for large values of  $\hat{u}_2$ , as well as  
 606 the region of very large positive tendency  $(1/\hat{u}_1)d\hat{u}_1/dt$  in Fig. 10(b) are determined by the other  
 607 terms. As a result, the equilibration of the flow in the upper layer branch is due to the nonlinear  
 608 interaction of the two mean flow components  $\hat{u}_1$  and  $\hat{u}_2$  rather than the energy correction that  
 609 underlies the equilibration of the flow in the lower branch.

## 610 7. Eckhaus instability of the side band jets

611 In this section we study the stability of the sideband jet equilibria. As noted by Parker and  
 612 Krommes (2014), these harmonic jet equilibria are susceptible to Eckhaus instability, a well known  
 613 result for harmonic equilibria of the G–L equation (Hoyle 2006). Here, we present the main results  
 614 of the Eckhaus instability and compare them with fully nonlinear S3T dynamics.

615 a. An intuitive view of the Eckhaus instability

616 To obtain intuition for the eddy–mean flow dynamics underlying the Eckhaus instability, note  
617 first that the G–L dynamics are given by the balance between the vorticity flux feedback  $f_r(v) =$   
618  $f_r(0) - c_2 v^2$ , which provides a diffusive correction to the original up-gradient fluxes  $f_r(0) > 0$  at  
619  $n_c$ , and the stabilizing nonlinear term  $c_3 |A|^2$ . Let us assume an equilibrium jet with  $v > 0$ , i.e.  
620 with a scale smaller than that of the most unstable jet at  $n_c$ , and also assume a sinusoidal phase  
621 perturbation:

$$A(Y) = R_0 e^{i[vY + \eta \sin(qY)]} \quad \text{with} \quad \eta \ll 1. \quad (52)$$

622 Figure 12 shows how the perturbed jet (52) is compressed for half the wavelength of the phase per-  
623 turbation  $\pi/q$  (unshaded region) and dilated for the other half (shaded region). In the compressed  
624 region the jet appears with an enhanced wavenumber  $v + \delta v$  while in the dilated region the jet  
625 appears with a reduced wavenumber  $v - \delta v$ . As a result, the vorticity flux feedback  $f_r(v)$  is larger  
626 in the dilated (shaded) region implying a tendency to enhance the jet; the opposite occurs in the  
627 compressed region (non-shaded). Figure 12 shows a qualitative sketch of the mean vorticity fluxes,  
628  $\overline{v' \zeta'}$ , that demonstrates this process. If the nonlinear term does not counteract this mismatch, the  
629 dilated part of the jet will grow and take over the whole domain thus producing a jet with lower  $v$ .  
630 (Similarly, for an equilibrium jet with  $v < 0$  there is a tendency for the compressed part of the jet  
631 to take over the whole domain producing a jet with larger  $v$ .)

632 To summarize, due to the diffusive nature of the vorticity flux feedback there is a tendency to go  
633 towards  $v = 0$  jets if not counteracted by the nonlinear eddy–mean flow feedback.

634 b. A formal view of the Eckhaus instability

635 To address quantitatively the stability of the harmonic jet equilibria (28), let us reformulate the  
 636 G–L equation by rewriting the jet amplitude  $A$  in polar form as:

$$A(Y, T) = R(Y, T) e^{i\Theta(Y, T)}, \quad (53)$$

637 where  $R$  is the amplitude and  $\Theta$  is the phase of the jet. The equilibrium jets have a constant  
 638 amplitude  $R_0(v)$  given by (28) and a linearly varying phase  $\Theta = vY$ . From (19), such equilibria  
 639 exist only for  $|v| < v_e = \sqrt{1/c_2}$ . Consider now small perturbations about this equilibrium jet:

$$R = R_0(v) + \hat{\rho} e^{iqY+\lambda T} \quad \text{and} \quad \Theta = vY + \hat{\phi} e^{iqY+\lambda T}. \quad (54)$$

640 As shown in Appendix D, we have exponential growth of these perturbations if

$$q^2 + 2(v_e^2 - 3v^2) < 0. \quad (55)$$

641 For an infinite domain the gravest mode has  $q = 0$  and therefore the jets with amplitude (53) are  
 642 Eckhaus unstable when  $|v| > v_e/\sqrt{3}$ . Maximum instability occurs for

$$|q|_{\max} = v_e \frac{\sqrt{3(v/v_e)^4 + 2(v/v_e)^2 - 1}}{2(v/v_e)}, \quad (56)$$

643 and therefore, the Eckhaus instability will form a jet of wavenumber  $n_c + \mu(v \pm |q|_{\max})$ . Figure  
 644 13(a) shows the wavenumber  $|q|_{\max}$  as a function of the equilibrium jet wavenumber  $v$ . Note that the equilibria with wavenumbers  $v \approx v_e/\sqrt{3}$  are unstable to jets with neighboring  
 645 wavenumbers as  $|q|_{\max} \ll 1$ , while equilibria with wavenumbers  $v \approx v_e$  are unstable to the jet  
 646 with wavenumber  $n_c$  as  $|q|_{\max} \approx 1$ .

647 The growth rate for the most unstable structure with  $|q|_{\max}$  is

$$\lambda_{\max} = \frac{(3v^2 - v_e^2)^2}{4c_1 v_e^2 v^2}. \quad (57)$$

648 and is shown in Fig. 13(b).

650 c. Comparison with S3T dynamics

651 Compare first the stability analysis for the harmonic jets derived in the weakly nonlinear limit of  
 652 G–L dynamics to nonlinear dynamics in the S3T system. Note that the growth rate of the Eckhaus  
 653 instability is much less than the corresponding growth rate of the flow-forming instability of the  
 654 homogeneous state of a jet for almost all wavenumbers  $v$ . Figure 13(b) compares the growth  
 655 rate  $\lambda_{max}$  for the perturbation with  $|q|_{max}$  that will eventually form a jet with wavenumber  $n_c +$   
 656  $\mu(v \pm |q|_{max})$  to the growth rate of the flow-forming instability of the homogeneous equilibrium  
 657 that will form a jet with the same wavenumber (shown with dashed line). As a result, the weak  
 658 Eckhaus instability manifests only in carefully contrived S3T simulations; any simulation of the  
 659 S3T system (5) starting from a random initial perturbation at low supercriticality will evolve into  
 660 the most unstable jet with wavenumber  $n_c$ .

661 Second, in contrast with the infinite domain, for the doubly periodic box the first side band  
 662 jets appear when  $v \geq v^\pm$ , while the gravest wavenumber  $q$  is  $q_{min} \stackrel{\text{def}}{=} 1/(\mu k_{f*} L_*)$ . Therefore, the  
 663 instability criterion (55) is satisfied for

$$\mu \leq \frac{\sqrt{(3 - 1/2)c_2}}{k_{f*} L_*}. \quad (58)$$

664 We compare here the stability boundary (58) with the stability analysis based on the nonlinear  
 665 S3T dynamics. The stability of the inhomogeneous jet–turbulence S3T equilibria shown in Fig. 7  
 666 is studying using the numerical methods developed by Constantinou (2015); Constantinou et al.  
 667 (2016); for the stability boundary (58) we use the effective values  $c_2^{\text{ex}\pm}$  for the side-band jet equi-  
 668 libria with  $v^\pm$ . Unstable (stable) equilibria are shown in Fig. 7 with open (filled) symbols, while  
 669 the stability boundaries for  $v^\pm$  are shown with the vertical dotted lines. For  $\beta_6$ , the parabolic pro-  
 670 file of the eigenvalue relation, on which the Eckhaus instability calculations are based, remains  
 671 accurate for larger supercriticalities and, therefore, the stability boundary (58) consists a good

approximation. For larger and smaller values of  $\beta$ , the parabolic profile is not so accurate and, therefore, the criterion developed fails. For example, for both  $\beta_1$  and  $\beta_{192}$  all the  $v^+$  jet equilibria are unstable.

Last, we compare the development of the Eckhaus instability as predicted by the G–L dynamics (27) and as predicted by the S3T dynamics. Figure 14 shows the evolution of the slightly perturbed  $n_* = 5$  ( $v^-$ ) and  $n_* = 7$  ( $v^+$ ) equilibria for  $\beta_6$  and supercriticality  $\mu = 0.3$  obtained from integrations of the S3T system (5). In both cases, the equilibria are unstable to  $q = q_{\min}$  perturbations. As the instability develops the  $\hat{u}(k_{y*} = 6)$  component of the flow grows exponentially (panels (c) and (d)) and the flow moves into the stable  $n_* = 6$  ( $n_c$ ) equilibrium jet by branching or merging (panels (a) and (b)). We compute the growth rate of the Eckhaus instability from (D4) by substituting  $v = q = 1/(\mu k_{f*} L_*)$  and using the effective values  $c_2^{\text{ex}\pm}$ :

$$\lambda^\pm = \mu^2 \frac{-1 + \sqrt{[(\mu^{\text{ex}\pm}/\mu)^2 - 1]^2 + 4(\mu^{\text{ex}\pm}/\mu)^4}}{c_1}. \quad (59)$$

Panels (c) and (d) demonstrate that the growth rate obtained by (59) is in excellent agreement with the growth rate of the Eckhaus instability in the nonlinear simulations. Furthermore, the equilibrium jet amplitude is accurately predicted by (29).

Figure 15 shows the comparison of the growth rates for the other unstable sideband jet equilibria illustrated in Fig. 7. We see once more that for  $\beta_6$ , for which the parabolic approximation of the eigenvalue relation used to obtain the G–L dynamics is accurate, the growth rates agree for almost all the unstable range. For  $\beta_1$  and  $\beta_{192}$ , for which the parabolic profile is not accurate, there is in general disagreement.

691 **8. Conclusion**

692 We examined the dynamics that underlies the formation and support of zonal jets at finite am-  
693 plitude in forced–dissipative barotropic beta-plane turbulence using the statistical state dynamics  
694 of the turbulent flow closed at second-order. Within this framework, jet formation is shown to  
695 arise as a flow-forming instability (or ‘zonostrophic instability’) of the homogeneous statistical  
696 equilibrium turbulent state when the non-dimensional parameter  $\varepsilon = \varepsilon_*/(k_{f*}^{-2}r_*^3)$  crosses a certain  
697 critical threshold  $\varepsilon_c$ . In this work, we studied the dynamics that govern the equilibration of the  
698 flow-forming instability in the limit of small supercriticality  $\mu = \sqrt{\varepsilon/\varepsilon_c - 1}$ .

699 When supercriticality  $\mu \ll 1$ , the growth rate of the unstable modes as a function of the mean  
700 flow wavenumber is to a good approximation a parabola. This allows a two-time, two-scale ap-  
701 proximation of the nonlinear dynamics resulting in the weakly nonlinear Ginzburg–Landau dy-  
702 namics for the evolution of zonal jets. The equilibration of the flow-forming instability, was ex-  
703 tensively investigated using the G–L dynamics. Also, the predictions of the weakly nonlinear G–L  
704 dynamics regarding (i) the amplitude of the equilibrated jets and (ii) their stability were compared  
705 to the fully nonlinear S3T dynamics for a wide range of values for the non-dimensional parameter  
706  $\beta = \beta_*/(k_{f*}r_*)$ .

707 According to G–L dynamics, the harmonic unstable modes of the homogeneous equilibrium  
708 state equilibrate at finite amplitude. The predicted amplitude of the jet that results from the equili-  
709 bration of the most unstable mode with wavenumber  $n_c$ , was compared to the amplitude of the jet  
710 equilibria of the nonlinear S3T dynamics. For  $\beta \lesssim 20$ , the jet amplitude was found to be accurately  
711 predicted by the G–L dynamics for up to  $\mu \approx 0.2$ . For  $\beta \gtrsim 20$ , a new branch of jets with much  
712 larger amplitudes was discovered that was distinctly different from the G–L branch of jet equilib-  
713 ria. The bifurcation diagram (e.g., Fig. 6) exhibits a classic cusp bifurcation with hysteretic loops.

714 The new branch of jet equilibria exists even at *subcritical values* of the flow-forming instability  
715 of the homogeneous state (i.e., for  $\varepsilon < \varepsilon_c$ ). This has two consequences: first, continuation meth-  
716 ods for finding equilibria converge only for small supercriticalities, as the jet equilibria transition  
717 discontinuously to the upper branch (see, e.g., Fig. 6(a)). This explains the failure to converge  
718 to equilibria reported by Parker and Krommes (2014). Second, the cusp bifurcation allows the  
719 emergence of jets at subcritical parameter values through a nonlinear flow-forming instability.

720 We compared the amplitudes of the jets that emerge from the side-band jet-instabilities of the  
721 most unstable mode of the flow-forming instability (i.e., the jets that emerge at scales  $n_{c*} \pm 1/L_*$ ).

722 The amplitude predicted by the G–L equation is partially based on the parabolic approximation  
723 to the dispersion relation and, more specifically, on the curvature of the function of the growth  
724 rate at criticality. This approximation was found to be valid away from criticality only for non-  
725 dimensional  $\beta \approx 5$  and as a result the predicted amplitude fails outside this range. We propose a  
726 way to remedy this discrepancy (at least to some extend) by using the exact values for the curva-  
727 ture of the growth rate function for larger supercriticalities instead of the curvature given by the  
728 parabolic approximation (see, e.g., Fig. 14). With this modification, the side-band jet amplitudes  
729 can be predicted by the G–L dynamics close to their onset for  $\beta \lesssim 1$  and for a wide range of su-  
730 percriticalities for  $\beta \approx 5$ . For  $\beta \gtrsim 20$ , apart from the G–L branch the additional branch of higher  
731 amplitude side-band jets was also found.

732 The physical and dynamical processes underlying the equilibration of the flow-forming insta-  
733 bility were then examined using three methods. The first was the decomposition of the nonlinear  
734 term in the G–L equation governing the equilibration of the instability in two terms. One involves  
735 the change in the homogeneous part of the eddy covariance that is required by total energy con-  
736 servation. The other involves the vorticity flux feedback resulting from the interaction of the most  
737 unstable jet with wavenumber  $n_c$  and the jet with the double harmonic  $2n_c$  that is inevitably gener-

738 ated by the nonlinear interactions. The second was the method of Bakas et al. (2015) for separating  
739 the contributions of the various eddies in the induced vorticity fluxes: both for the linear term in  
740 the G–L equation that drives the instability, and also for the nonlinear term that stabilizes the flow.  
741 In this way, the eddies yielding up-gradient fluxes and the eddies yield down-gradient fluxes were  
742 identified along with the change in the up-gradient or down-gradient character of the fluxes that  
743 occurs as the jets grow. The third method was the development of a reduced dynamical system  
744 that retains the fully nonlinear interactions in contrast to the G–L equation. This reduced system  
745 is based on an adiabatic assumption for the covariance changes and on a Galerkin truncation of  
746 the dynamics retaining only the  $n_c$  and  $2n_c$  components of the mean flow that play important role  
747 in the equilibration of the zonostrophic instability.

748 For the G–L branch, the central physical process responsible for the equilibration is the reduction  
749 in the up-gradient vorticity flux that occurs through the change in the homogeneous part of the  
750 eddy covariance. For low values of  $\beta$ , the instability is quickly quenched and the jets equilibrate  
751 at low amplitude. The reason is that the contribution of the eddies that induce up-gradient fluxes  
752 and drive the instability is weakened as the jets emerge while simultaneously the contribution of  
753 the eddies that induce down-gradient fluxes is increased. As a result, the jets equilibrate at a small  
754 amplitude and are supported by the same eddies that drive the instability.

755 For large values of  $\beta$ , both the up-gradient and the down-gradient contributions are almost  
756 equally weakened thus leading to a slow decay of the growth rate and to an equilibrated jet with a  
757 much larger amplitude. Because the equilibrium amplitude is large, the stabilizing fluxes that are  
758 multiplied by the square of the jet amplitude in the G–L equation are dominant and, therefore, at  
759 equilibrium the jet is supported by the eddies that were initially hindering its growth (these eddies  
760 have phase lines that form small angles with the meridional but different than zero).

761 For the new branch of jet equilibria the main physical process responsible for the equilibration  
762 is the interaction of the  $n_c$  and the  $2n_c$  component of the emerging flow. Starting from a finite  
763 amplitude jet with either strong  $n_c$  or  $2n_c$  components, this nonlinear interaction leads to rapid  
764 growth of the jet and to equilibration of the flow at amplitudes much larger than the G–L branch  
765 and with much stronger  $2n_c$  component.

766 Finally, the stability of the equilibrated side band unstable jet perturbations was examined. For  
767 an infinite domain, zonal jets with scales close to the scale  $n_c$  of the most unstable mode of the  
768 flow-forming instability are stable; jets with scales much larger or much smaller are unstable.  
769 The incipient Eckhaus instability of the harmonic equilibria of the G–L equation is well studied  
770 within the literature of pattern formation but here it was interpreted in a physically intuitive way.  
771 The equilibrated jets have a low amplitude (proportional to the supercriticality) and therefore do  
772 not significantly change the structure of the turbulence. As a result, a mean flow perturbation  
773 on the turbulent flow induces approximately the same vorticity flux feedback as in the absence  
774 of any jet with the vorticity flux feedback having a maximum at the most unstable wavenumber.  
775 Therefore, when a dilation–compression phase perturbation is inserted in the equilibrated jet that  
776 has a different wavenumber than  $n_c$ , the vorticity flux feedback for the dilated or the compressed  
777 part of the jet will be larger and this part of the jet tends to grow and take over the whole domain.

778 The predictions for the stability boundary and the growth rate of the Eckhaus instability were  
779 then compared to the stability analysis of the jet equilibria using the fully nonlinear S3T system  
780 and the methods developed in Constantinou (2015). For  $\beta \approx 5$ , using the exact values for the  
781 curvature of the growth rate function yields accurate predictions for both the stability boundary  
782 and the growth rate. As the instability develops the unstable side band jets with smaller/larger  
783 scale than the jet with wavenumber  $n_c$  branch/merge into the stable  $n_c$  jet. For low or high values

784 of  $\beta$ , large quantitative discrepancies occur with a few exceptions, but the qualitative picture of  
785 the dynamics with branching/merging into the stable jet equilibrium remains.

786 We note that the comparison of the G-L dynamics with nonlinear S3T integrations, as well as  
787 investigation of the equilibration process with an anisotropic ring forcing showed that the results  
788 in this study are not sensitive to the forcing structure.

789 A question that rises naturally is whether the results discussed here are relevant for strong tur-  
790 bulent jets. Strong turbulent jets also undergo bifurcations as the turbulence intensity increases.

791 There are, however, qualitative differences compared to weak jets: strong jets *always* merge to  
792 larger scales while weak jets can either merge or branch to reach a scale close to  $n_c$ . Based on  
793 the relevant dynamics in pattern formation, we expect that the anti-diffusive phase dynamics that  
794 are involved in the Eckhaus instability will play a significant role in the secondary instabilities of  
795 large-amplitude jets as well. Moreover, the generalization of the Ginzburg–Landau dynamics that  
796 we have put forward in this study (eqs. (40)) is able to describe the slow evolution of a jet that  
797 consists of more than just one harmonic. This generalization of the Ginzburg–Landau dynamics,  
798 we hope, will provide a vehicle for understanding the dynamics involving bifurcations of strong  
799 turbulent jets.

800 *Acknowledgments.* The authors would like to thank Jeffrey B. Parker for helpful comments on  
801 the first version of the manuscript. N.A.B. was supported by the AXA Research Fund. N.C.C. was  
802 partially supported by the NOAA Climate and Global Change Postdoctoral Fellowship Program,  
803 administered by UCAR’s Cooperative Programs for the Advancement of Earth System Sciences  
804 and also by the National Science Foundation under Award OCE-1357047.

805 APPENDIX A

806 **S3T formulation and eigenvalue relation of the flow-forming instability**

807 In this appendix we derive the eigenvalue relation of the flow-forming instability. The eigenvalue  
 808 relation was first derived by Srinivasan and Young (2012). Here, we repeat the derivation mainly  
 809 to introduce some notation and terminology that will prove to be helpful in understanding the  
 810 nonlinear equilibration of the flow-forming instability.

811 Consider the S3T system (5), where

$$\mathcal{L} \stackrel{\text{def}}{=} \beta (\partial_{x_a} \Delta_a^{-1} + \partial_{x_b} \Delta_b^{-1}) + 2 , \quad (\text{A1})$$

812 is the operator governing the linear eddy dynamics,

$$\mathcal{N}(\bar{u}, C) \stackrel{\text{def}}{=} [-\bar{u}_a \partial_{x_a} + (\partial_{y_a}^2 \bar{u}_a) \partial_{x_a} \Delta_a^{-1} - \bar{u}_b \partial_{x_b} + (\partial_{y_b}^2 \bar{u}_b) \partial_{x_b} \Delta_b^{-1}] C , \quad (\text{A2})$$

813 is the nonlinear operator governing the eddy–mean flow interaction and

$$\mathcal{R}(C) \stackrel{\text{def}}{=} \frac{1}{2} [(\partial_{x_a} \Delta_a^{-1} + \partial_{x_b} \Delta_b^{-1}) C]_{a=b} , \quad (\text{A3})$$

814 is the eddy vorticity flux driving the mean flow. Subscripts  $a$  or  $b$  on operators acting on  $C$  indicate  
 815 the point of evaluation and the specific independent variable the operator is acting on, and the  
 816 subscript  $a = b$  indicates that the function of  $x_a$  and  $x_b$ , e.g., inside the square brackets on the  
 817 right-hand-side of (A3), is transformed into a function of a single variable by setting  $x_a = x_b = x$ .

818 The eigenvalue relation is obtained by linearizing the S3T system (5) about the homogeneous  
 819 equilibrium (8). Then, introducing the ansatz (9) in the linearized S3T equations we obtain:

$$(\sigma + 1) \delta \bar{u} = \mathcal{R}(\delta C) , \quad (\text{A4a})$$

$$(\sigma + \mathcal{L}) \delta C = \mathcal{N}(\delta \bar{u}, C^e) . \quad (\text{A4b})$$

820 The quantity:

$$f(\sigma | \delta \bar{u}, C) \stackrel{\text{def}}{=} \mathcal{R} [(\sigma + \mathcal{L})^{-1} \mathcal{N}(\delta \bar{u}, C)] , \quad (\text{A5})$$

821 is the vorticity flux induced by the distortion of the incoherent homogeneous eddy equilibrium  
 822 field with covariance  $C$  by the mean flow  $\delta \bar{u}$ .

823 The inversion of the operators and the algebra is simplified by taking the Fourier decomposition  
 824 of  $\tilde{C}_n^{(h)}$ :

$$\tilde{C}_n^{(h)}(\mathbf{x}_a - \mathbf{x}_b) = \int \frac{d^2\mathbf{k}}{(2\pi)^2} \hat{C}(\mathbf{k}) e^{i\mathbf{k}\cdot(\mathbf{x}_a - \mathbf{x}_b)}. \quad (\text{A6})$$

825 By inserting (A6) and (8) into (A4b) we obtain:

$$\delta C = \varepsilon e^{in(y_a+y_b)/2} [G^+(\sigma, \mathbf{x}_a - \mathbf{x}_b) - G^-(\sigma | \mathbf{x}_a - \mathbf{x}_b)], \quad (\text{A7})$$

826 where we defined

$$G^\pm(\sigma | \mathbf{x}) \stackrel{\text{def}}{=} \int \frac{d^2\mathbf{k}}{(2\pi)^2} \frac{ik_x k_\pm^2 (k_\pm^2 - n^2)}{(\sigma + 2) k_+^2 k_-^2 + 2i\beta n k_x k_y} \frac{\hat{Q}(\mathbf{k}_\pm)}{2} e^{i\mathbf{k}\cdot\mathbf{x}}, \quad (\text{A8})$$

827 with  $\mathbf{k}_\pm = \mathbf{k} + \mathbf{n}/2$ ,  $\mathbf{n} = (0, n)$  and  $k_\pm = |\mathbf{k}_\pm|$ . Inserting (A7) in (A4a) we obtain (10), in which

$$f = \int \frac{d^2\mathbf{k}}{(2\pi)^2} \frac{nk_x^2(k_y + n/2)(1 - n^2/k^2)}{(\sigma + 2)k^2 k_s^2 + 2i\beta nk_x(k_y + n/2)} \hat{Q}(\mathbf{k}), \quad (\text{A9})$$

828 with  $k_s \stackrel{\text{def}}{=} |\mathbf{k} + \mathbf{n}|$ . After substituting the ring forcing power spectrum (4), expressing the integrand  
 829 in polar coordinates  $(k_x, k_y) = (k \cos \vartheta, k \sin \vartheta)$  and integrating over  $k$  (A9) becomes:

$$f = \int_0^{2\pi} \frac{N_f d\theta}{(\sigma + 2)D_f + i\beta D_\beta}, \quad (\text{A10})$$

830 with  $N_f(\theta) = n \cos^2 \theta (\sin \vartheta + n/2)(1 - n^2)/\pi$ ,  $D_f(\vartheta) = \cos^2 \vartheta + (\sin \vartheta + n)^2$  and  $D_\beta(\vartheta) =$   
 831  $2n \cos \vartheta (\sin \vartheta + n/2)$ . At criticality ( $\sigma = 0$ ), using the mirror symmetry property of the forcing,  
 832 i.e.,  $\hat{Q}(-k_x, k_y) = \hat{Q}(k_x, k_y)$ , the vorticity flux feedback is rewritten as:

$$f_r = \int_0^{\pi/2} \mathcal{F}(\vartheta, n) d\vartheta, \quad (\text{A11})$$

833 where

$$\mathcal{F}(\vartheta, n) = \frac{N_f(\vartheta)D_f(\vartheta)}{4D_f^2(\vartheta) + \beta^2 D_\beta^2(\vartheta)} + \frac{N_f(\vartheta + \pi)D_f(\vartheta + \pi)}{4D_f^2(\vartheta + \pi) + \beta^2 D_\beta^2(\vartheta + \pi)}, \quad (\text{A12})$$

834 is the contribution to the feedback from the waves with wavevectors  $(k_x, k_y)$ ,  $(-k_x, -k_y)$  and their  
 835 mirror symmetric wavevectors  $(-k_x, k_y)$  and  $(k_x, -k_y)$  respectively.

837 **Ginzburg–Landau equation for the weakly nonlinear evolution of a zonal jet perturbation**  
 838 **about the homogeneous state**

839 To obtain the G–L equation governing the nonlinear S3T dynamics near the onset of the insta-  
 840 bility, we assume that the energy input rate is slightly supercritical  $\varepsilon = \varepsilon_c(1 + \mu^2)$ , where  $\mu \ll 1$   
 841 measures the supercriticality. As discussed in section 4, the emerging jet grows slowly at a rate  
 842  $O(\mu^2)$  and contains a band of wavenumbers of  $O(\mu)$  around  $n_c$ , where  $n_c$  is the wavenumber of  
 843 the jet that achieves neutrality at  $\varepsilon_c$ . Therefore, we assume that the dynamics evolve on a slow  
 844 time scale  $T = \mu^2 t$  and are modulated at a long meridional scale  $Y = \mu y$ . The leading order jet is  
 845  $\bar{u}_1 = A(Y, T) e^{i n_c y}$ . We then expand the velocity and the covariance as a series in  $\mu$ :

$$\bar{u} = \mu \bar{u}_1(y, Y, T) + \mu^2 \bar{u}_2(y, Y, T) + O(\mu^3), \quad (\text{B1a})$$

$$C = C^e(x_a - x_b) + \mu C_1(x_a - x_b, Y_a, Y_b, T) + \mu^2 C_2(x_a - x_b, Y_a, Y_b, T) + O(\mu^3), \quad (\text{B1b})$$

846 along with the linear and nonlinear operators  $\mathcal{L}$  and  $\mathcal{N}$  that depend on the fast and slow merid-  
 847 ional coordinates,  $y$  and  $Y$  respectively.

848 We substitute (B1) in (5) and collect terms with equal powers of  $\mu$ . As discussed in section 4, we  
 849 further assume that the amplitude  $A$ , as well as  $C_1$  and  $C_2$ , are independent of the slow coordinate  $Y$ .  
 850 This way operators  $\mathcal{L}$  and  $\mathcal{N}$  also become independent of  $Y$ . In this case, the order  $\mu^0$  terms yield  
 851 the homogeneous equilibrium. Terms of order  $\mu^1$  yield the balance:

$$\mathcal{A} \begin{pmatrix} \bar{u}_1 \\ C_1 \end{pmatrix} \stackrel{\text{def}}{=} \begin{pmatrix} \bar{u}_1 - \mathcal{R}(C_1) \\ \mathcal{L}C_1 - \mathcal{N}(\bar{u}_1, C^e) \end{pmatrix} = 0, \quad (\text{B2})$$

852 which can also be compactly written as

$$\bar{u}_1 = \varepsilon_c f(0 | \bar{u}_1, Q/2), \quad (\text{B3})$$

853 where  $f(\sigma|\bar{u}_1, Q/2)$  is the vorticity flux feedback on the mean flow  $\bar{u}_1$  as defined in (A5). The  
 854 solution of (B3) is the eigenfunction of operator  $\mathcal{A}$  with zero eigenvalue:

$$\begin{pmatrix} \bar{u}_1 \\ C_1 \end{pmatrix} = A(T) \begin{pmatrix} e^{in_c y} \\ \varepsilon_c e^{in_c(y_a+y_b)/2} [G_c^+(0|\mathbf{x}_a - \mathbf{x}_b) - G_c^-(0|\mathbf{x}_a - \mathbf{x}_b)] \end{pmatrix} + \text{c.c.} \quad (\text{B4})$$

855 In (B4) the subscript  $c$  on  $G^\pm$  denotes that they are evaluated at  $n = n_c$ . At order  $\mu^2$  the balance is:

$$\mathcal{A} \begin{pmatrix} \bar{u}_2 \\ C_2 \end{pmatrix} = \begin{pmatrix} 0 \\ \mathcal{N}(\bar{u}_1, C_1) + \varepsilon_c Q \end{pmatrix}. \quad (\text{B5})$$

856 Equation (B5) has a homogeneous solution which is proportional to  $[\bar{u}_1, C_1]^T$  and can be incorpo-  
 857 rated in it, and a particular solution. The nonlinear term  $\mathcal{N}(\bar{u}_1, C_1)$  generates both a double and a  
 858 zero harmonic mean flow (and covariance). As a result, the particular solution is:

$$\begin{pmatrix} \bar{u}_2 \\ C_2 \end{pmatrix} = \begin{pmatrix} 0 \\ \varepsilon_c Q(\mathbf{x}_a - \mathbf{x}_b)/2 + C_{20}(\mathbf{x}_a - \mathbf{x}_b, T) \end{pmatrix} + \begin{pmatrix} \alpha_2 A(T)^2 e^{2in_c y} \\ C_{22}(\mathbf{x}_a - \mathbf{x}_b, T) e^{2in_c(y_a+y_b)/2} \end{pmatrix} + \text{c.c.}, \quad (\text{B6})$$

859 where  $C_{20}$  and  $C_{22}$  are the zero and double harmonic coefficients of the covariance and

$$\alpha_2 \stackrel{\text{def}}{=} \frac{\frac{\varepsilon_c}{2} \int \frac{d^2 k}{(2\pi)^2} \frac{in_c k_x^3 (k^2 - n_c^2)}{k^2 k_2^2 + i\beta n_c k_x k_{y,1}} \left\{ \frac{k_{y,2}(k_2^2 - n_c^2)}{k^2 k_4^2 + 2i\beta n_c k_x k_{y,2}} - \frac{k_y k_2^2 (k^2 - n_c^2)}{k^2 (k_2^2 k_4^2 + 2i\beta n_c k_x k_{y,2})} \right\} \hat{Q}(\mathbf{k})}{\varepsilon_c \int \frac{d^2 k}{(2\pi)^2} \frac{n_c k_x^2 k_{y,2} (k^2 - 4n_c^2)}{k^2 (k^2 k_4^2 + 2i\beta n_c k_x k_{y,2})} \hat{Q}(\mathbf{k}) - 1}, \quad (\text{B7})$$

860 with  $k_{y,j} \stackrel{\text{def}}{=} k_y + j n_c / 2$  and  $k_j^2 \stackrel{\text{def}}{=} k_x^2 + k_{y,j}^2$  for any integer  $j$ .

861 At order  $\mu^3$  the balance is:

$$\mathcal{A} \begin{pmatrix} \bar{u}_3 \\ C_3 \end{pmatrix} = \begin{pmatrix} -\partial_T \bar{u}_1 \\ -\partial_T C_1 + \mathcal{N}(\bar{u}_2, C_1) + \mathcal{N}(\bar{u}_1, C_2) \end{pmatrix}. \quad (\text{B8})$$

862 If the right-hand-side of (B8) is an eigenvector of operator  $\mathcal{A}$  with zero eigenvalue then secular  
 863 terms appear that produce a mean flow and an associated covariance that are unbounded at  $|y| \rightarrow \infty$ .

<sup>864</sup> This occurs when

$$-\partial_T \bar{u}_1 + \mathcal{R} \left\{ \mathcal{L}^{-1} [-\partial_T C_1 + \mathcal{N}(\bar{u}_2, C_1) + \mathcal{N}(\bar{u}_1, C_2)] \right\} \quad (\text{B9})$$

<sup>865</sup> has a non-zero  $e^{in_c y}$  component. The secular terms vanish if:

$$\partial_T \bar{u}_1 + \mathcal{R} (\mathcal{L}^{-1} \partial_T C_1) = f(0 | \bar{u}_1, C^e) + f(0 | \bar{u}_1, C_{20}) + \mathcal{P}_1 \left[ f(0 | \bar{u}_1, C_{22} e^{2in_c(y_a+y_b)/2} + \text{c.c.}) + f(0 | \bar{u}_2, C_1) \right] . \quad (\text{B10})$$

<sup>866</sup> where  $\mathcal{P}_1$  is the operator that projects onto the harmonic  $n_c$ :

$$\mathcal{P}_1 g(y) \stackrel{\text{def}}{=} \int_{-\infty}^y g(s) e^{in_c(y-s)} ds . \quad (\text{B11})$$

<sup>867</sup> Equation (B10) determines the equilibration of the most unstable jet. The terms on the right-  
<sup>868</sup> hand-side of (B10) are nonlinear in  $\bar{u}$  and  $C$  and they are responsible for the equilibration of the  
<sup>869</sup> SSD instability. Let us take a closer look into each term in (B10). The second term on the left-  
<sup>870</sup> hand-side of (B10) is:

$$\mathcal{R} (\mathcal{L}^{-1} \partial_T C_1) = (\partial_T A) (c_1 - 1) e^{in_c y} , \quad (\text{B12})$$

<sup>871</sup> where

$$c_1 = 1 + \frac{\epsilon_c}{4} \int \frac{d^2 k}{(2\pi)^2} \frac{n_c k_x^2 k_{y,1} k_2^2 (k^2 - n_c^2)}{(k^2 k_2^2 + i\beta n_c k_x k_{y,1})^2} \hat{Q}(k) . \quad (\text{B13})$$

<sup>872</sup> The first term on the right-hand-side of (B10) is the vorticity flux feedback on  $\bar{u}_1$  at criticality

$$f(0 | \bar{u}_1, C^e) = A e^{in_c y} . \quad (\text{B14})$$

<sup>873</sup> The second term on the right-hand-side of (B10) is the vorticity flux feedback between the order  
<sup>874</sup>  $\mu^1$  mean jet  $\bar{u}_1$ , and the homogeneous order  $\mu^2$  eddy covariance  $C_{20}$ :

$$f(0 | \bar{u}_1, C_{20}) = -c_3^{ec} A |A|^2 e^{in_c y} , \quad (\text{B15})$$

<sup>875</sup> with

$$c_3^{ec} \stackrel{\text{def}}{=} \frac{\epsilon_c}{4} \int \frac{d^2 k}{(2\pi)^2} \frac{n_c k_x^4 k_2^2 (k_2^2 - n_c^2)(k^2 - n_c^2)^2}{|k^2 k_2^2 + i\beta n_c k_x k_{y,1}|^2} \left[ \frac{2k_{y,1}}{k^2 k_2^2 + i\beta n_c k_x k_{y,1}} - \frac{k_{y,-1}}{k^2 k_{-2}^2 + i\beta n_c k_x k_{y,-1}} - \frac{k_{y,3}}{k_2^2 k_4^2 + i\beta n_c k_x k_{y,3}} \right] \hat{Q}(k) . \quad (\text{B16})$$

876 The third term on the right-hand-side of (B10) is the  $e^{in_c y}$  component of the vorticity flux feedback  
 877 between the jet  $\bar{u}_1$ , with wavenumber  $n_c$  and the jet  $\bar{u}_2$  with wavenumber  $2n_c$  with the inhomoge-  
 878 neous eddy covariance  $C_1$  and  $C_{22}$ :

$$\mathcal{P}_1 \left[ f(0|\bar{u}_1, C_{22} e^{2in_c(y_a+y_b)/2} + \text{c.c.}) + f(0|\bar{u}_2, C_1) \right] = -c_3^{1,2} A |A|^2 e^{in_c y}, \quad (\text{B17})$$

879 with

$$\begin{aligned} c_3^{1,2} &\stackrel{\text{def}}{=} \frac{\varepsilon_c}{8} \int \frac{d^2 k}{(2\pi)^2} \left\{ \frac{n_c k_x^4 k^2 (k^2 - n_c^2)(k_2^2 - n_c^2)}{[k^2 k_4^2 + 2i\beta n_c k_x k_{y,2}] [k^2 k_2^2 + i\beta n_c k_x k_{y,1}]} \left[ \frac{k_{y,1}(k_4^2 - n_c^2)}{k^2 k_2^2 + i\beta n_c k_x k_{y,1}} - \frac{k_{y,3} k_4^2 (k^2 - n_c^2)}{k^2 (k_2^2 k_4^2 + i\beta n_c k_x k_{y,3})} \right] \right. \\ &\quad \left. + \frac{n_c k_x^4 k_{y,1} k_2^2 (k_{-2}^2 - n_c^2)(k^2 - n_c^2)^2 (k_{-2}^2 k_2^2 + i\beta n_c k_x k_y)}{(k^2 k_2^2 + i\beta n_c k_x k_{y,1})^2 (k^2 k_{-2}^2 + i\beta n_c k_x k_{y,-1})(k_{-2}^2 k_2^2 + 2i\beta n_c k_x k_y)} \right\} \hat{Q}(\mathbf{k}) \\ &+ i a_2 \frac{\varepsilon_c}{4} \int \frac{d^2 k}{(2\pi)^2} \left\{ \frac{k^2 - 4n_c^2}{k^2 k_4^2 + 2i\beta n_c k_x k_{y,2}} \left[ \frac{k_{y,1}(k_4^2 - n_c^2)}{k^2 k_2^2 + i\beta n_c k_x k_{y,1}} - \frac{k_{y,3} k_4^2 (k^2 - n_c^2)}{k^2 (k_2^2 k_4^2 + i\beta n_c k_x k_{y,3})} \right] \right. \\ &\quad \left. + \frac{k^2 - n_c^2}{k^2 k_2^2 - i\beta n_c k_x k_{y,1}} \left[ \frac{k_{y,-1}(k_2^2 - 4n_c^2)}{k^2 k_{-2}^2 + i\beta n_c k_x k_{y,-1}} - \frac{k_{y,3} k_2^2 (k^2 - 4n_c^2)}{k^2 (k_2^2 k_4^2 + i\beta n_c k_x k_{y,3})} \right] \right\} n_c k_x^3 \hat{Q}(\mathbf{k}). \end{aligned} \quad (\text{B18})$$

880 Therefore, using (B12), (B14), (B15) and (B17) we get that (B10) reduces to:

$$c_1 \partial_T A = A - c_3 A |A|^2, \quad (\text{B19})$$

881 where  $c_3 \stackrel{\text{def}}{=} c_3^{ec} + c_3^{1,2}$ .

882 Finally, we arrive to the G–L equation (27) by adding the diffusion term  $c_2 \partial_Y^2 A$  on the right-  
 883 hand-side of (B19), with

$$\begin{aligned} c_2 &\stackrel{\text{def}}{=} -\frac{\varepsilon_c}{2} \left( \frac{\partial^2 f}{\partial n^2} \right)_{n_c, \sigma=0} \\ &= \frac{\varepsilon_c}{2} \int \frac{d^2 k}{(2\pi)^2} \left[ \frac{k_x^2 k_{y,2}^2 k^2 (k^2 - n_c^2)(2k^2 + i\beta k_x)}{(k^2 k_2^2 + i\beta n_c k_x k_{y,1})^3} - \frac{k_x^2 k^2 (k^2 - 4n_c k_y - 5n_c^2)}{2(k^2 k_2^2 + i\beta n_c k_x k_{y,1})^2} + \frac{n_c k_x^2 k_{y,1}}{k^2 (k^2 k_2^2 + i\beta n_c k_x k_{y,1})} \right] \hat{Q}(\mathbf{k}). \end{aligned} \quad (\text{B20})$$

884 The coefficients  $c_1$ ,  $c_2$  and  $c_3$  are all functions of  $\beta$ ,  $n_c$  and the forcing covariance spectrum,  $\hat{Q}$ .  
 885 For the ring forcing (4) considered here they are all real and positive.

886 To study the contribution to each of the components of  $c_3$  from the forced waves with phase  
 887 lines forming an angle  $\vartheta$  with the  $y$ -axis, we substitute the ring forcing power spectrum (4). After  
 888 expressing the integrand in polar coordinates  $(k_x, k_y) = (k \cos \vartheta, k \sin \vartheta)$  and integrate over  $k$  we  
 889 obtain:

$$[c_3^{ec}, c_3^{1,2}, c_3] = \varepsilon_c \int_0^{\pi/2} [\mathcal{F}_{ec}, \mathcal{F}_{1,2}, \mathcal{F}_{NL}] d\vartheta , \quad (B21)$$

890 where  $\mathcal{F}_{ec}$ ,  $\mathcal{F}_{1,2}$ , and  $\mathcal{F}_{NL}$  is the contribution of the waves with  $(k_x, k_y)$ ,  $(-k_x, -k_y)$  and their mir-  
 891 ror symmetric  $(-k_x, k_y)$  and  $(k_x, -k_y)$  to the feedbacks and  $\mathcal{F}_{NL} = \mathcal{F}_{ec} + \mathcal{F}_{1,2}$ . Figure B10 shows  
 892 these contributions as a function of wave angle. For  $\beta \ll 1$ , forced eddies at all angles contribute  
 893 positively to both  $\mathcal{F}_{ec}$  and  $\mathcal{F}_{1,2}$ . The eddies tend to reduce the positive destabilizing contribu-  
 894 tion  $\mathcal{F} > 0$  at small angles mainly through  $\mathcal{F}_{1,2}$ , while they enhance the negative stabilizing contribu-  
 895 tion  $\mathcal{F} < 0$  at large angles mainly through  $\mathcal{F}_{ec}$ . For  $\beta \gg 1$ , the dominant contribution comes from  
 896  $\mathcal{F}_{ec}$  and it follows roughly the same pattern as  $\mathcal{F}$ . That is, due to the reduction in their energy  
 897 the eddies tend to reduce both the up-gradient vorticity fluxes of waves with angles  $|\vartheta| \lesssim \vartheta_0$  and  
 898 the down-gradient fluxes of waves with phase lines at angles  $|\vartheta| \gtrsim \vartheta_0$  with the latter reduction  
 899 being larger. As a result, the nonlinear feedback of eddies with phase lines at angles  $|\vartheta| \gtrsim \vartheta_0$  is to  
 900 enhance the jet and, as discussed in section 4, these are the eddies that support the equilibrated jet.

## APPENDIX C

### Non-isotropic ring forcing

902 Here we briefly discuss the effect of the forcing anisotropy on the obtained results. Consider the  
 903 generalization of forcing (4) with spectrum:  
 904

$$\hat{Q}_*(\mathbf{k}_*) = 4\pi k_{f*} \delta(k_* - k_{f*}) [1 + \gamma \cos(2\vartheta)] , \quad (C1)$$

905 where  $\vartheta \stackrel{\text{def}}{=} \arctan(k_{y*}/k_{x*})$  and  $|\gamma| \leq 1$  so that  $\hat{Q}_* \geq 0$ . Parameter  $\gamma$  determines the degree of  
 906 anisotropy of the forcing (Srinivasan and Young 2014; Bakas et al. 2015). The isotropic case  
 907 of (4) is recovered for  $\gamma = 0$ . For example, for  $\gamma = 1$  we get an anisotropic forcing that favors  
 908 structures with small  $|k_{y*}|$  (i.e., favoring structures like that in Fig. 2(a) compared to structures like  
 909 that in Fig. 2(b)), as if the vorticity injection was due to baroclinic growth processes. All three  
 910 coefficients  $c_1$ ,  $c_2$ , and  $c_3$  in (27) are real and positive for forcing (C1).

911 We first note that we obtain similar results to the isotropic forcing case regarding the comparison  
 912 of the G-L predictions to the fully nonlinear dynamics (not shown). That is, both the existence of  
 913 the upper branch equilibria, as well as the relative quantitative success of the G-L dynamics (after  
 914 the proposed modifications) in predicting the amplitude and instability of the equilibrated jets are  
 915 insensitive to forcing structure.

916 Regarding the physical processes underlying the equilibration of the jets, we show in Fig. 17(a)  
 917 the amplitude  $R_0$  for the equilibrated most unstable jet as a function of  $\beta$ . For  $\beta \gg 1$ , the amplitude  
 918 has the same power law as in the isotropic forcing case shown in Fig. 8(a). However, the amplitude  
 919 shows different dependence with  $\beta$  for  $\beta \ll 1$  but, however, this regime is of no interest since for  
 920 as  $\beta \rightarrow 0$  no zonal jets emerge in (1) anyway. The relative contribution of the eddy-correction term  
 921 and the interaction of  $n_c$  with the double harmonic jet in  $c_3$  is shown in Fig. 17(b). Similarly to the  
 922 isotropic forcing case, for most values of  $\beta$  the equilibration is dominated by the interaction of the  
 923 most unstable jet with the homogeneous covariance correction.

924 Lastly, we note that for anisotropic forcing similar qualitative decomposition of  $c_3$  from various  
 925 waves (as in Fig. 9) also occurs (not shown).

926 APPENDIX D

927 **Eckhaus stability of G–L dynamics**

928 To address the Eckhaus instability of the harmonic jet equilibria, we rewrite the jet amplitude  $A$   
 929 in polar form (53), we then substitute into (27) and separate real and imaginary parts to obtain:

$$c_1 \partial_T R = [1 + c_2 \partial_Y^2 - c_2 (\partial_Y \Theta)^2] R - c_3 R^3, \quad (\text{D1a})$$

$$c_1 R \partial_T \Theta = 2c_2 (\partial_Y R) (\partial_Y \Theta) + c_2 R \partial_Y^2 \Theta. \quad (\text{D1b})$$

930

931 Assume now an equilibrium jet with constant amplitude  $R_0(v)$  and a linearly varying phase  
 932  $\Theta = vY$ . Consider small perturbations about this equilibrium jet:

$$R = R_0(v) + \rho \quad \text{and} \quad \Theta = vY + \phi, \quad (\text{D2})$$

933 and linearize (D1) to obtain:

$$c_1 \partial_T \rho = [1 + c_2(\partial_Y^2 - v^2) - 3c_3 R_0^2] \rho - 2c_2 R_0 v \partial_Y \phi, \quad (\text{D3a})$$

$$c_1 R_0 \partial_T \phi = 2c_2 v \partial_Y \rho + c_2 R_0 \partial_Y^2 \phi. \quad (\text{D3b})$$

934 Using the ansatz  $[\rho, \phi] = [\hat{\rho}, \hat{\phi}] e^{iqY + \lambda T}$  we find that the eigenvalues  $\lambda$  are:

$$\lambda = \frac{v^2 - v_e^2 - q^2 \pm \sqrt{(v^2 - v_e^2)^2 + 4q^2 v^2}}{c_1 v_e^2}. \quad (\text{D4})$$

935 Instability occurs when  $\lambda > 0$ , that is when

$$q^2 + 2(v_e^2 - 3v^2) < 0. \quad (\text{D5})$$

## 936 References

- 937 Ait-Chaalal, F., T. Schneider, B. Meyer, and J. B. Marston, 2016: Cumulant expansions for atmo-  
 938 spheric flows. *New. J. Phys.*, **18** (2), 025 019, doi:10.1088/1367-2630/18/2/025019.
- 939 Bakas, N. A., N. C. Constantinou, and P. J. Ioannou, 2015: S3T stability of the homo-  
 940 geneous state of barotropic beta-plane turbulence. *J. Atmos. Sci.*, **72** (5), 1689–1712, doi:  
 941 10.1175/JAS-D-14-0213.1.

- 942 Bakas, N. A., and P. J. Ioannou, 2013a: Emergence of large scale structure in barotropic  $\beta$ -plane  
943 turbulence. *Phys. Rev. Lett.*, **110**, 224501, doi:10.1103/PhysRevLett.110.224501.
- 944 Bakas, N. A., and P. J. Ioannou, 2013b: On the mechanism underlying the spontaneous emergence  
945 of barotropic zonal jets. *J. Atmos. Sci.*, **70** (7), 2251–2271, doi:10.1175/JAS-D-12-0102.1.
- 946 Bakas, N. A., and P. J. Ioannou, 2014: A theory for the emergence of coherent structures in beta-  
947 plane turbulence. *J. Fluid Mech.*, **740**, 312–341, doi:10.1017/jfm.2013.663.
- 948 Bakas, N. A., and P. J. Ioannou, 2018: Is spontaneous generation of coherent baroclinic flows  
949 possible? *J. Fluid Mech.*, (in review, arXiv:1712.05724).
- 950 Bakas, N. A., and P. J. Ioannou, 2019: Emergence of non-zonal coherent structures. *Zonal jets*,  
951 B. Galperin, and P. L. Read, Eds., Cambridge University Press, chap. 27, (arXiv:1501.05280).
- 952 Bouchet, F., C. Nardini, and T. Tangarife, 2013: Kinetic theory of jet dynamics in the stochastic  
953 barotropic and 2D Navier-Stokes equations. *J. Stat. Phys.*, **153** (4), 572–625, doi:10.1007/  
954 s10955-013-0828-3.
- 955 Chen, S., R. E. Ecke, G. L. Eyink, M. Rivera, M. Wan, and Z. Xiao, 2006: Physical mech-  
956 anism of the two-dimensional inverse energy cascade. *Phys. Rev. Lett.*, **96**, 084502, doi:  
957 10.1103/PhysRevLett.96.084502.
- 958 Constantinou, N. C., 2015: Formation of large-scale structures by turbulence in rotating plan-  
959 ets. Ph.D. thesis, National and Kapodistrian University of Athens, Athens, URL <http://www.didaktorika.gr/eadd/handle/10442/35501?locale=en>, (also available at arXiv:1503.07644).
- 960 Constantinou, N. C., B. F. Farrell, and P. J. Ioannou, 2014a: Emergence and equilibration of jets  
961 in beta-plane turbulence: applications of Stochastic Structural Stability Theory. *J. Atmos. Sci.*,  
962 **71** (5), 1818–1842, doi:10.1175/JAS-D-13-076.1.

- 964 Constantinou, N. C., B. F. Farrell, and P. J. Ioannou, 2016: Statistical state dynamics of jet–  
965 wave coexistence in barotropic beta-plane turbulence. *J. Atmos. Sci.*, **73** (5), 2229–2253, doi:  
966 10.1175/JAS-D-15-0288.1.
- 967 Constantinou, N. C., A. Lozano-Durán, M.-A. Nikolaidis, B. F. Farrell, P. J. Ioannou, and  
968 J. Jiménez, 2014b: Turbulence in the highly restricted dynamics of a closure at second order:  
969 comparison with DNS. *J. Phys. Conf. Ser.*, **506**, 012 004, doi:10.1088/1742-6596/506/1/012004.
- 970 Constantinou, N. C., and J. B. Parker, 2018: Magnetic suppression of zonal flows on a beta plane.  
971 *Astrophys. J.*, **863** (1), 46, doi:10.3847/1538-4357/aace53.
- 972 Cross, M., and H. Greenside, 2009: *Pattern formation and dynamics in nonequilibrium systems*.  
973 Cambridge University Press, 552 pp.
- 974 Danilov, S., and D. Gurarie, 2004: Scaling, spectra and zonal jets in beta-plane turbulence. *Phys.*  
975 *Fluids*, **16**, 2592–2603, doi:10.1063/1.1752928.
- 976 Farrell, B. F., and P. J. Ioannou, 2003: Structural stability of turbulent jets. *J. Atmos. Sci.*, **60**,  
977 2101–2118, doi:10.1175/1520-0469(2003)060<2101:SSOTJ>2.0.CO;2.
- 978 Farrell, B. F., and P. J. Ioannou, 2007: Structure and spacing of jets in barotropic turbulence. *J.*  
979 *Atmos. Sci.*, **64**, 3652–3665, doi:10.1175/JAS4016.1.
- 980 Farrell, B. F., and P. J. Ioannou, 2009: Emergence of jets from turbulence in the shallow-  
981 water equations on an equatorial beta plane. *J. Atmos. Sci.*, **66**, 3197–3207, doi:10.1175/  
982 2009JAS2941.1.
- 983 Farrell, B. F., and P. J. Ioannou, 2017: Statistical state dynamics based theory for the formation  
984 and equilibration of Saturn’s north polar jet. *Phys. Rev. Fluids*, **2** (7), 073 801, doi:10.1103/  
985 PhysRevFluids.2.073801.

- 986 Farrell, B. F., P. J. Ioannou, J. Jiménez, N. C. Constantinou, A. Lozano-Durán, and M.-A. Niko-  
987 laidis, 2016: A statistical state dynamics-based study of the structure and mechanism of large-  
988 scale motions in plane Poiseuille flow. *J. Fluid Mech.*, **809**, 290–315, doi:10.1017/jfm.2016.661.
- 989 Farrell, B. F., P. J. Ioannou, and M. A. Nikolaidis, 2017: Instability of the roll–streak structure  
990 induced by background turbulence in pretransitional Couette flow. *Phys. Rev. Fluids*, **2** (3),  
991 034 607, doi:10.1103/PhysRevFluids.2.034607.
- 992 Fitzgerald, J. G., and B. F. Farrell, 2018a: Statistical State Dynamics of vertically sheared hor-  
993 izontal flows in two-dimensional stratified turbulence. *J. Fluid Mech.*, **854**, 544–590, doi:  
994 10.1017/jfm.2018.560.
- 995 Fitzgerald, J. G., and B. F. Farrell, 2018b: Vertically sheared horizontal flow-forming instability in  
996 stratified turbulence: Analytical linear stability analysis of Statistical State Dynamics equilibria.  
997 *J. Atmos. Sci.*, doi:10.1175/JAS-D-18-0075.1, in press.
- 998 Frishman, A., and C. Herbert, 2018: Turbulence statistics in a 2D vortex condensate. *Phys. Rev.*  
999 *Lett.*, **120**, 204 505, doi:10.1103/PhysRevLett.120.204505.
- 1000 Frishman, A., J. Laurie, and G. Falkovich, 2017: Jets or vortices – what flows are generated by an  
1001 inverse turbulent cascade? *Phys. Rev. Fluids*, **2**, 032 602, doi:10.1103/PhysRevFluids.2.032602.
- 1002 Holloway, G., 2010: Eddy stress and shear in 2-D flows. *J. Turbul.*, **11**, N14, doi:10.1080/  
1003 14685248.2010.481673.
- 1004 Hoyle, R., 2006: *Pattern formation: An introduction to methods*. Cambridge University Press.
- 1005 Huang, H.-P., and W. A. Robinson, 1998: Two-dimensional turbulence and persistent zonal jets in  
1006 a global barotropic model. *J. Atmos. Sci.*, **55**, 611–632, doi:10.1175/1520-0469(1998)055<0611:  
1007 TDTAPZ>2.0.CO;2.

- <sup>1008</sup> Ingersoll, A. P., 1990: Atmospheric dynamics of the outer planets. *Science*, **248**, 308–315, doi:  
<sup>1009</sup> 10.1126/science.248.4953.308.
- <sup>1010</sup> Ingersoll, A. P., and Coauthors, 2004: Dynamics of Jupiter's atmosphere. *Jupiter: the planet, satel-*  
<sup>1011</sup> *lites, and magnetosphere*, F. Bagenal, T. E. Dowling, and W. B. McKinnon, Eds., Cambridge  
<sup>1012</sup> University Press, Cambridge, 105–128.
- <sup>1013</sup> Kraichnan, R. H., 1976: Eddy viscosity in two and three dimensions. *J. Atmos. Sci.*, **33** (8), 1521–  
<sup>1014</sup> 1536, doi:10.1175/1520-0469(1976)033<1521:EVITAT>2.0.CO;2.
- <sup>1015</sup> Manfroi, A. J., and W. R. Young, 1999: Slow evolution of zonal jets on the beta plane. *J. Atmos.*  
<sup>1016</sup> *Sci.*, **56**, 784–800, doi:10.1175/1520-0469(1999)056<0784:SEOZJO>2.0.CO;2.
- <sup>1017</sup> Marston, J. B., G. P. Chini, and S. M. Tobias, 2016: Generalized quasilinear approximation: Ap-  
<sup>1018</sup> plication to zonal jets. *Phys. Rev. Lett.*, **116** (21), 214501 EP –5, doi:10.1103/PhysRevLett.116.  
<sup>1019</sup> 214501.
- <sup>1020</sup> Marston, J. B., E. Conover, and T. Schneider, 2008: Statistics of an unstable barotropic jet from a  
<sup>1021</sup> cumulant expansion. *J. Atmos. Sci.*, **65** (6), 1955–1966, doi:10.1175/2007JAS2510.1.
- <sup>1022</sup> Marston, J. B., W. Qi, and S. M. Tobias, 2014: Direct statistical simulation of a jet. *Zonal jets:*  
<sup>1023</sup> *Phenomenology, genesis, physics*, B. Galperin, and P. L. Read, Eds., Cambridge University  
<sup>1024</sup> Press, chap. 5, (submitted, arXiv:1412.0381).
- <sup>1025</sup> Parker, J. B., and J. A. Krommes, 2013: Zonal flow as pattern formation. *Phys. Plasmas*, **20**,  
<sup>1026</sup> 100703, doi:10.1063/1.4828717.
- <sup>1027</sup> Parker, J. B., and J. A. Krommes, 2014: Generation of zonal flows through symmetry breaking of  
<sup>1028</sup> statistical homogeneity. *New J. Phys.*, **16** (3), 035006, doi:10.1088/1367-2630/16/3/035006.

- 1029 Read, P. L., and Coauthors, 2007: Dynamics of convectively driven banded jets in the laboratory.  
1030 *J. Atmos. Sci.*, **64**, 4031–4052, doi:10.1175/2007JAS2219.1.
- 1031 Rhines, P. B., 1975: Waves and turbulence on a beta-plane. *J. Fluid Mech.*, **69**, 417–433, doi:  
1032 10.1017/S0022112075001504.
- 1033 Salyk, C., A. P. Ingersoll, J. Lorre, A. Vasavada, and A. D. Del Genio, 2006: Interaction between  
1034 eddies and mean flow in Jupiter’s atmosphere: Analysis of Cassini imaging data. *Icarus*, **185**,  
1035 430–442, doi:10.1016/j.icarus.2006.08.007.
- 1036 Shepherd, T. G., 1987: Rossby waves and two-dimensional turbulence in a large-scale zonal jet. *J.*  
1037 *Fluid Mech.*, **183**, 467–509, doi:10.1017/S0022112087002738.
- 1038 Simonnet, E., and F. Bouchet, 2016: Computing rare transitions between zonal mid-latitude jets.  
1039 *EGU General Assembly Conference Abstracts*, EGU General Assembly Conference Abstracts,  
1040 Vol. 18, EPSC2016–7415, URL <http://adsabs.harvard.edu/abs/2016EGUGA..18.7415S>.
- 1041 Srinivasan, K., and W. R. Young, 2012: Zonostrophic instability. *J. Atmos. Sci.*, **69** (5), 1633–1656,  
1042 doi:10.1175/JAS-D-11-0200.1.
- 1043 Srinivasan, K., and W. R. Young, 2014: Reynold stress and eddy difusivity of  $\beta$ -plane shear flows.  
1044 *J. Atmos. Sci.*, **71** (6), 2169–2185, doi:10.1175/JAS-D-13-0246.1.
- 1045 Starr, V. P., 1968: *Physics of negative viscosity phenomena*. McGraw Hill, New York, 256 pp.
- 1046 Thomas, V., B. K. Lieu, M. R. Jovanović, B. F. Farrell, P. J. Ioannou, and D. F. Gayme, 2014:  
1047 Self-sustaining turbulence in a restricted nonlinear model of plane Couette flow. *Phys. Fluids*,  
1048 **26**, 105 112, doi:10.1063/1.4898159.
- 1049 Tobias, S. M., K. Dagon, and J. B. Marston, 2011: Astrophysical fluid dynamics via direct numer-  
1050 ical simulation. *Astrophys. J.*, **727**, 127, doi:10.1088/0004-637X/727/2/127.

- 1051 Tobias, S. M., and J. B. Marston, 2013: Direct statistical simulation of out-of-equilibrium jets.
- 1052 *Phys. Rev. Lett.*, **110** (10), 104 502, doi:10.1103/PhysRevLett.110.104502.
- 1053 Vallis, G. K., and M. E. Maltrud, 1993: Generation of mean flows and jets on a beta-plane and  
1054 over topography. *J. Phys. Oceanogr.*, **23**, 1346–1362, doi:10.1175/1520-0485(1993)023<1346:  
1055 GOMFAJ>2.0.CO;2.
- 1056 Vasavada, A. R., and A. P. Showman, 2005: Jovian atmospheric dynamics: an update after *Galileo*  
1057 and *Cassini*. *Rep. Prog. Phys.*, **68**, 1935–1996, doi:10.1088/0034-4885/68/8/R06.

## LIST OF TABLES

1058	<b>Table 1.</b> Exact values of non-dimensional planetary vorticity gradient $\beta \stackrel{\text{def}}{=} \beta_*/(k_{f*}r_*)$ used in the S3T simulations of section 5 and their corresponding values of the dimensional critical wavenumber $n_{c*}$ .	57
1059		
1060		
1061		

1062 TABLE 1. Exact values of non-dimensional planetary vorticity gradient  $\beta \stackrel{\text{def}}{=} \beta_*/(k_{f*}r_*)$  used in the S3T  
 1063 simulations of section 5 and their corresponding values of the dimensional critical wavenumber  $n_{c*}$ .

Notation	$\beta$	$n_{c*}$
$\beta_1$	1.1915	8
$\beta_3$	3.0235	7
$\beta_6$	6.2761	6
$\beta_{12}$	12.136	5
$\beta_{24}$	24.576	4
$\beta_{58}$	58.137	3
$\beta_{192}$	192.62	2

## 1064 LIST OF FIGURES

- 1065 **Fig. 1.** Second-order closure can captures the mean flow dynamics despite differences in structure  
1066 of eddy spectra. Here shown are the energy spectra for a fully nonlinear simulation (eq. (1))  
1067 and its quasilinear approximation (i.e., employing the second-order closure). Both simulation  
1068 form 4 strong jets of similar strength. Setup as described in section 5 with  $\beta/(k_f r) = 70$   
1069 and  $\varepsilon/(k_f^2 r^3) = 4 \times 10^5$ . Contours in logarithmic scale and the same for both panels. . . . . 61
- 1070 **Fig. 2.** Waves with small  $|k_y|$  (as in panel (a)) produce up-gradient vorticity fluxes that destabilize  
1071 any mean flow perturbation superimposed on the homogeneous turbulent equilibrium; waves with large  $|k_y|$  (as in panel (b)) produce down-gradient vorticity fluxes that tend to  
1072 diminish mean flow perturbations. . . . . 62
- 1073
- 1074 **Fig. 3.** The contribution  $\mathcal{F}$  to the vorticity flux feedback  $f_r$  for the most unstable jet eigenfunction  
1075 from the waves with phase lines inclined at angle  $\vartheta$  with respect to the meridional (solid  
1076 curves). Panel (a) shows the case with  $\beta = 0.1$  while panel (b) for  $\beta = 100$ . In panel (a)  
1077 the angle  $\vartheta = \arcsin[\frac{1}{2}(1+n^2)^{1/2}]$  that separates the waves with positive (destabilizing) and  
1078 negative (stabilizing) contribution to the vorticity flux feedback for  $\beta = 0$  is indicated with  
1079 a filled circle. Also, dashed curves show the contribution  $\mathcal{F}_{NL}$  to the nonlinear Landau  
1080 coefficient  $c_3$  for the most unstable jet eigenfunction as a function of the wave angle  $\vartheta$  (see  
1081 section 6). . . . . 63
- 1082 **Fig. 4.** Validity of the approximate eigenvalue relation (17). (a) Comparison of the growth rates for  
1083 jet perturbations with wavenumber  $v$  as predicted by the exact eigenvalue relation (10) (solid curve)  
1084 and by the parabolic approximation (17) (dashed curve) for supercriticality  $\mu = 0.5$   
1085 and  $\beta = 1$ . Circles mark the maximum growth rate: for (10) this is at wavenumber  $n_{\max}$ ,  
1086 while for (17) at  $n_c$ . (b) Same as panel (a) but for  $\beta = 100$ . (c) The difference between  
1087 the exact wavenumber of maximum growth  $n_{\max}$  and the approximate wavenumber of max-  
1088 imum growth  $n_c$  as a function of the supercriticality  $\mu$ . (d) The relative difference between  
1089 the exact growth rate  $\sigma$  for a jet at wavenumber  $n_c$  and the approximate growth rate  $\mu^2/c_1$  as  
1090 a function of supercriticality  $\mu$ . (e) The exact growth rate of jet perturbations with wavenum-  
1091 bers  $v_e$  and  $-v_e$  as a function of  $\beta$  for supercriticality  $\mu = 0.5$ . The parabolic approximation  
1092 predicts zero growth for these marginal wavenumbers. . . . . 64
- 1093 **Fig. 5.** The amplitude  $\mu A$  of the equilibrated most unstable jet with wavenumber  $n_c$  as a function  
1094 of supercriticality  $\mu$  for four values of  $\beta$ . The G-L branch is shown with circles  $\circ$ ; the  
1095 upper branch (which appears for  $\beta \gtrsim 20$ ) is shown with triangles  $\triangle$ . Solid lines show the  
1096 jet amplitude as predicted by the G-L (cf. (29)). . . . . 65
- 1097 **Fig. 6.** The bifurcation diagram for  $\beta_{58}$  (case shown in panel (c) of Fig. 5). (a) The amplitude  $\mu A$  of  
1098 the equilibrated most unstable jet with wavenumber  $n_c$  as a function of the energy input rate.  
1099 Squares denote the homogeneous equilibrium, circles the lower branch predicted by the G-L  
1100 dynamics and the triangles the upper branch of equilibria. Open symbols denote unstable jet  
1101 equilibria with respect to S3T dynamics; filled symbols denote stable jet equilibria. Multiple  
1102 stable equilibria exist for  $0.89 \leq \varepsilon/\varepsilon_c \leq 1.068$ . A comparison of the jet equilibrium structure  
1103 and the jet spectra for  $\varepsilon = 1.0025$  (which corresponds to  $\mu = 0.05$ ) is shown in panels (b)-  
1104 (d). Panels (b), (d) show the lower G-L branch jet; Panels (c), (e) show the upper branch jet.  
1105 In panel (d) the amplitude prediction for  $n_c$  by (29) and for  $2n_c$  by (22a) is also shown (open  
1106 circles). . . . . 65
- 1107 **Fig. 7.** The amplitude  $\mu A$  of the equilibrated unstable jets with wavenumbers  $n_c - 1/(\mu k_f * L_*)$  (di-  
1108 amonds) and  $n_c + 1/(\mu k_f * L_*)$  (squares) as a function of supercriticality  $\mu$  for four values  
1109 of  $\beta$ . The dashed lines show the amplitude predicted by the G-L dynamics (cf. (29)), while

1110 the solid lines show the amplitude predicted by the G–L dynamics with  $c_2^{\text{ex}\pm}$  as described  
 1111 in the text. Stable (unstable) equilibria are denoted with filled (empty) symbols and the  
 1112 vertical dotted lines show the stability boundary (58) obtained from the G–L dynamics (see  
 1113 section 7). . . . .

66

1114 **Fig. 8.** (a) The amplitude  $R_0(0) = 1/\sqrt{c_3}$  of the equilibrated most unstable jet with wavenumber  
 1115  $n_c$  as a function of  $\beta$ . Dashed lines show the  $\beta^{1/3}$  and  $\beta^{2/3}$  slopes for reference. (b) The  
 1116 coefficient  $c_3$  and its decomposition into the contributions  $c_3^{\text{ec}}$  and  $c_3^{1,2}$  as a function of  $\beta$ .  
 1117 Coefficient  $c_3^{1,2}$  is negative for  $4.9 \lesssim \beta \lesssim 79$ . However, for these values of  $c_3^{1,2}$  is at least an  
 1118 order of magnitude less than  $c_3^{\text{ec}}$  and, therefore, negligible. . . . .

67

1119 **Fig. 9.** (a) The contribution  $\mathcal{F}_{\text{NL}}$  to the coefficient  $c_3$  from waves at angle  $|\vartheta|$  in the limit of  $\beta \gg 1$ .  
 1120  $\mathcal{F}_{\text{NL}}$  assumes a dipole pattern. The amplitude of each of the dipole peaks scale with  $\beta$   
 1121 and the widths of the dipole structure scale with  $\beta^{-2/3}$ . For  $\beta \gg 1$  the structure of  $\mathcal{F}_{\text{NL}}$  is  
 1122 independent of the type of forcing used. (b) The contribution from waves at angle  $|\vartheta|$  to the  
 1123 finite amplitude equilibrium jet, as given by  $\mathcal{F} - R_0^2 \mathcal{F}_{\text{NL}}$  for three values of  $\beta$ . . . . .

68

1124 **Fig. 10.** The mean flow growth rates  $(1/\hat{u}_1)d\hat{u}_1/dt$  (panel (a)) and  $(1/\hat{u}_2)d\hat{u}_2/dt$  (panel (b)) ob-  
 1125 tained under an adiabatic approximation ( $\partial_t C = 0$ ) for a mean flow  $\bar{u} = \hat{u}_1 e^{in_c y} - \hat{u}_2 e^{2in_c y}$   
 1126 as a function of  $\hat{u}_1$  and  $\hat{u}_2$ . The thick curves are the zero tendency contours (solid curve  
 1127 for the  $d\hat{u}_1/dt$  and dashed for  $d\hat{u}_2/dt$ ). Infinitesimal jet perturbations start in the region in  
 1128 the  $\hat{u}_1$ – $\hat{u}_2$  phase space denoted as G–L and end up in the lower branch equilibrium shown  
 1129 by the filled circle. The arrows denote paths in the  $\hat{u}_1$ – $\hat{u}_2$  phase space that connect a finite  
 1130 amplitude jet perturbation starting from points A and B and ending up to the upper branch  
 1131 equilibrium, denoted by the filled triangle. (The paths were obtained by time-stepping the  
 1132 S3T system (5).) Panels (c)–(e) show the breakdown of the flux feedback  $\hat{f}_{n_c k_f^*}/\hat{u}_1$  into the  
 1133 components (c)  $f_{1,0}/\hat{u}_1$ , (d)  $f_{1,2}/\hat{u}_1$  and (e)  $f_{2,3}/\hat{u}_1$ . Similarly, panels (f)–(i) show the break-  
 1134 down of  $\hat{f}_{2 n_c k_f^*}/\hat{u}_2$  into the components (f)  $f_{2,0}/\hat{u}_2$ , (g)  $f_{1,1}/\hat{u}_2$ , (h)  $f_{1,3}/\hat{u}_2$  and (i)  $f_{2,4}/\hat{u}_2$ .  
 1135 Parameters used:  $\beta_{58}$  and supercriticality  $\mu = 0.1$ . . . . .

69

1136 **Fig. 11.** The locus of zero mean flow tendencies in  $\hat{u}_1$ – $\hat{u}_2$  space for various supercriticalities for the  
 1137 case with  $\beta_{58}$ . Jet equilibria exist at the intersection of the two loci, when  $d\hat{u}_1/dt = d\hat{u}_2/dt = 0$ . For (a)  $\varepsilon/\varepsilon_c = 0.84$  there is no intersection as only the homogeneous equilibrium is stable  
 1138 for  $\varepsilon/\varepsilon_c < 0.89$  (see Fig. 6(a)). For (b)  $\varepsilon/\varepsilon_c = 0.99$  there are two points of intersection that  
 1139 correspond to the stable and unstable upper branch equilibria that exist for  $0.89 < \varepsilon/\varepsilon_c < 1$ . For (c)  $\varepsilon/\varepsilon_c = 1.01$  there are three equilibria: two upper-branch equilibria (a stable and  
 1140 an unstable) and the lower-branch G–L equilibrium. For (d)  $\varepsilon/\varepsilon_c = 1.25$  only one upper  
 1141 branch equilibrium exists as the G–L branch and the unstable upper branch terminate at  
 1142  $\varepsilon/\varepsilon_c = 1.068$ . . . . .

70

1143 **Fig. 12.** Solid curve shows a sinusoidal equilibrium jet  $\bar{u}^e = R_0 \cos[(n_c + \mu v)y]$  with smaller scale  
 1144 ( $v = n_c$ ) compared to the scale of the most unstable jet (we take  $\mu = 1$  so that the  
 1145 wavenumber differences with the most unstable jet are exaggerated for illustration pur-  
 1146 poses). Dashed curve shows the resulting jet when the phase of the equilibrium jet  $\bar{u}^e$  is  
 1147 perturbed:  $\bar{u} = R_0 \cos[(n_c + \mu v)y + \eta \sin(qy)]$ , with  $q = v$  and  $\eta = 1/2$  (for illustration pur-  
 1148 poses). This perturbation dilates the jet in the shaded region and compresses the jet in the  
 1149 unshaded region. Dash-dotted curve is a qualitative depiction of the expected vorticity flux  
 1150 feedback  $v' \zeta'$  for the perturbed jet based on the dependence of  $f_r$  on the wavenumber  $v$ . . . . .

71

1151 **Fig. 13.** (a) The most unstable wavenumber for the Eckhaus instability,  $|q|_{\text{max}}/v_e$ , as a func-  
 1152 tion of the jet equilibrium wavenumber  $v/v_e$ . Instability occurs in the shaded region for

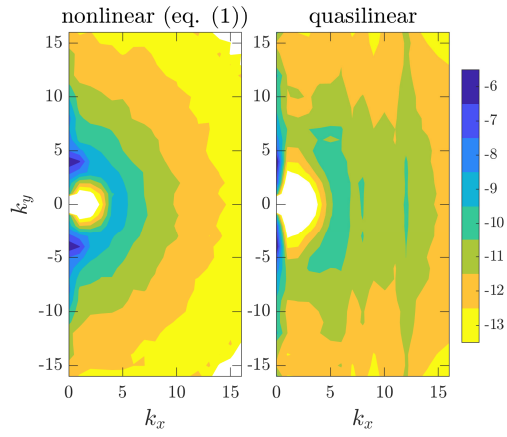
1155  $v/v_e > 1/\sqrt{3}$ . (b) The growth rate for the most Eckhaus unstable jet with  $q = q_{\max}$  (57) as  
1156 a function of the jet equilibrium wavenumber  $v$  (solid line). Also shown with dashed line  
1157 is the corresponding growth rate for the flow-forming instability of the jet with wavenum-  
1158 ber  $v \pm q_{\max}$  that will eventually be formed by the Eckhaus instability and is given by  
1159  $[1 - (v \pm q_{\max})^2/v_e^2]/c_1$ , according to the G-L equation (27). . . . . 72

1160 **Fig. 14.** The equilibration of the Eckhaus instability under S3T dynamics. Panel (a) shows the evo-  
1161 lution of the mean flow,  $\bar{u}_*(y, t)$ , for the slightly perturbed  $n_* = 5$  ( $v^-$ ) equilibrium. Panel  
1162 (c) shows the evolution of the  $n_* = 6$  Fourier component of the flow (solid). Also shown in  
1163 panel (b) are the growth rate predicted by (59) (dashed) and the amplitude of the  $n_* = 6$  jet as  
1164 predicted by (29) (dash-dot). Panels (b) and (d) show the same but for the slightly perturbed  
1165  $n_* = 7$  ( $v^+$ ) equilibrium. The planetary vorticity gradient is  $\beta_6$  and the supercriticality is  
1166  $\mu = 0.3$ . . . . . 73

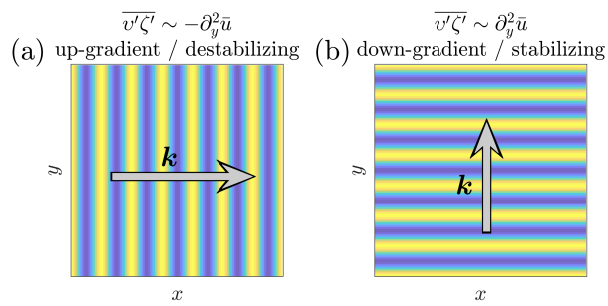
1167 **Fig. 15.** Growth rate for the Eckhaus instability of the finite amplitude jets. Shown is the growth rate  
1168 as a function of supercriticality  $\mu$  for three values of  $\beta$  obtained from the stability analysis  
1169 for the equilibrium jets with wavenumbers  $n_c - 1/(\mu k_{f*} L_*)$  (diamonds) and  $n_c + 1/(\mu k_{f*} L_*)$   
1170 (squares) using the fully nonlinear system (5). Dashed curves show the growth rate as pre-  
1171 dicted from the G-L dynamics; Solid curves show the growth rate (59) as predicted from the  
1172 G-L dynamics using the modified values for  $c_2$ , while dashed curves show the unmodified  
1173 growth rate (D4). . . . . 74

1174 **Fig. 16.** The contribution of the two feedbacks  $\mathcal{F}_{ec}$  (solid) and  $\mathcal{F}_{1,2}$  (dashed) to the nonlinear coef-  
1175 ficient  $\mathcal{F}_{NL}$ . Panel (a) shows the case with  $\beta = 0.1$  while panel (b) with  $\beta = 100$ . . . . . 75

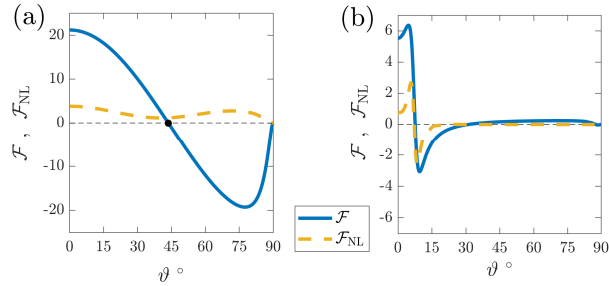
1176 **Fig. 17.** Same as Fig. 8 but for anisotropic forcing with  $\gamma = 1$ . (a) The amplitude  $R_0(0) = 1/\sqrt{c_3}$   
1177 of the equilibrated most unstable jet with wavenumber  $n_c$  as a function of  $\beta$  for the case  
1178 with isotropic ( $\gamma = 0$ ) and anisotropic ( $\gamma = 1$ ) forcing. Dashed line show the  $\beta^{1/3}$  slope for  
1179 reference. (b) The coefficient  $c_3$  and its decomposition into the contributions  $c_3^{ec}$  and  $c_3^{1,2}$  as  
1180 a function of  $\beta$ . . . . . 76



1181 FIG. 1. Second-order closure can captures the mean flow dynamics despite differences in structure of eddy  
 1182 spectra. Here shown are the energy spectra for a fully nonlinear simulation (eq. (1)) and its quasilinear approxi-  
 1183 mation (i.e., employing the second-order closure). Both simulation form 4 strong jets of similar strength. Setup  
 1184 as described in section 5 with  $\beta/(k_f r) = 70$  and  $\varepsilon/(k_f^2 r^3) = 4 \times 10^5$ . Contours in logarithmic scale and the same  
 1185 for both panels.



1186 FIG. 2. Waves with small  $|k_y|$  (as in panel (a)) produce up-gradient vorticity fluxes that destabilize any  
 1187 mean flow perturbation superimposed on the homogeneous turbulent equilibrium; waves with large  $|k_y|$  (as in  
 1188 panel (b)) produce down-gradient vorticity fluxes that tend to diminish mean flow perturbations.



1189 FIG. 3. The contribution  $\mathcal{F}$  to the vorticity flux feedback  $f_r$  for the most unstable jet eigenfunction from the  
 1190 waves with phase lines inclined at angle  $\vartheta$  with respect to the meridional (solid curves). Panel (a) shows the  
 1191 case with  $\beta = 0.1$  while panel (b) for  $\beta = 100$ . In panel (a) the angle  $\vartheta = \arcsin[\frac{1}{2}(1 + n^2)^{1/2}]$  that separates  
 1192 the waves with positive (destabilizing) and negative (stabilizing) contribution to the vorticity flux feedback for  
 1193  $\beta = 0$  is indicated with the filled circle. Also, dashed curves show the contribution  $\mathcal{F}_{NL}$  to the nonlinear Landau  
 1194 coefficient  $c_3$  for the most unstable jet eigenfunction as a function of the wave angle  $\vartheta$  (see section 6).

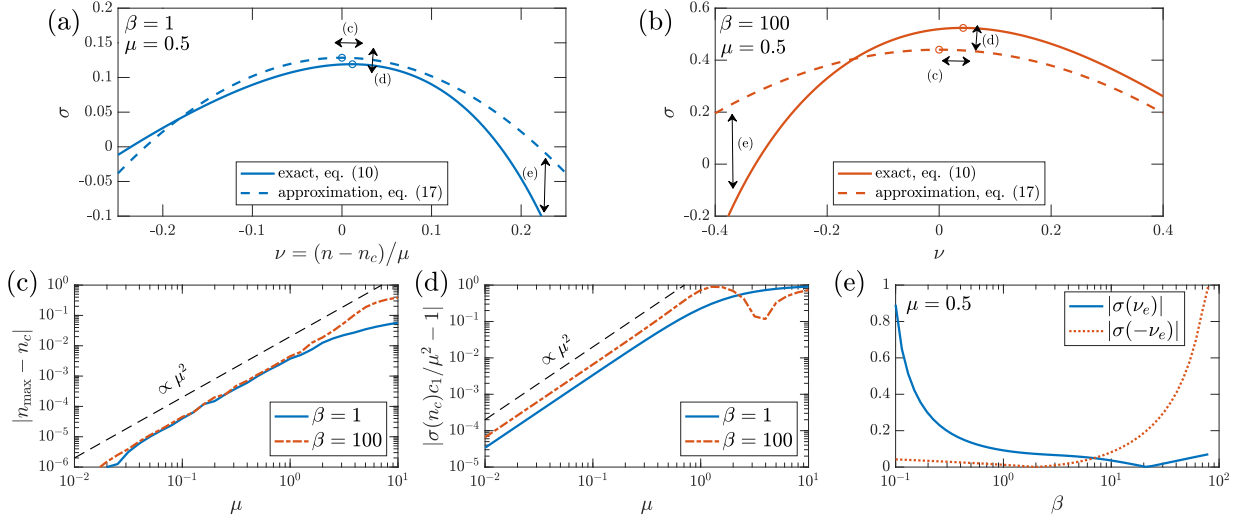
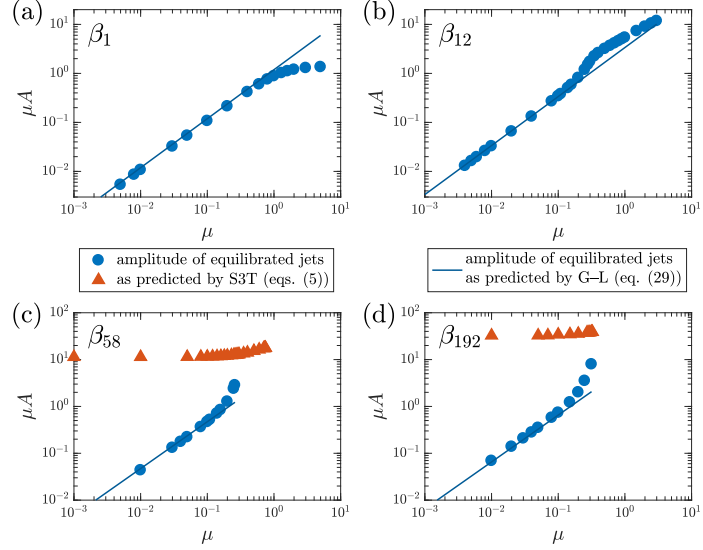
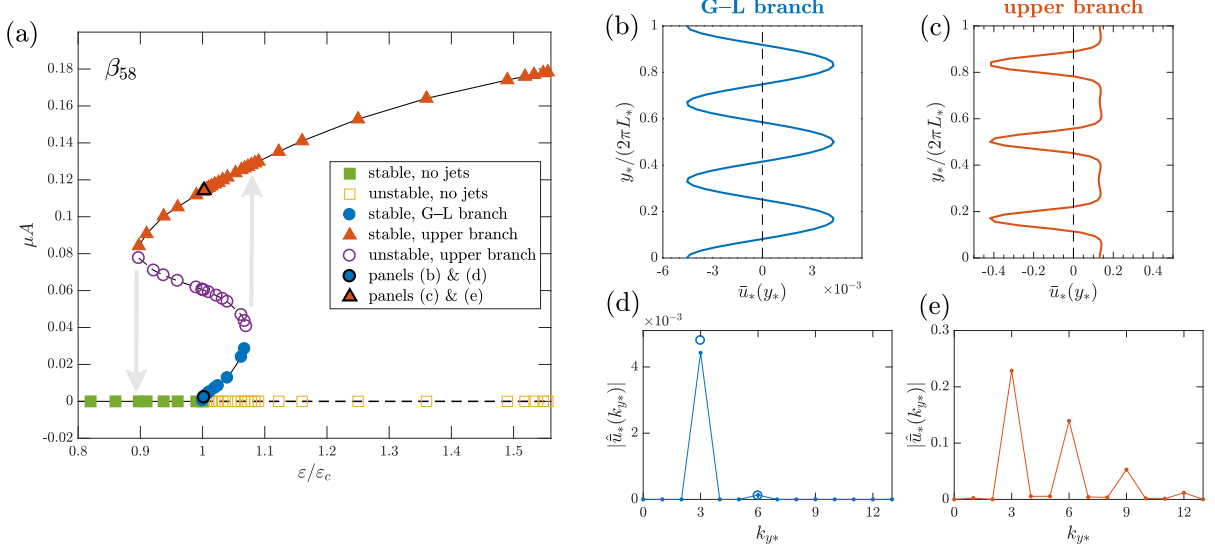


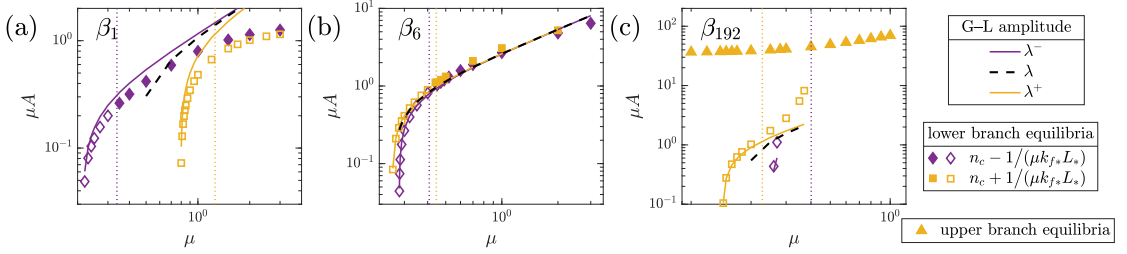
FIG. 4. Validity of the approximate eigenvalue relation (17). (a) Comparison of the growth rates for jet perturbations with wavenumber  $\nu$  as predicted by the exact eigenvalue relation (10) (solid curve) and by the parabolic approximation (17) (dashed curve) for supercriticality  $\mu = 0.5$  and  $\beta = 1$ . Circles mark the maximum growth rate: for (10) this is at wavenumber  $n_{\max}$ , while for (17) at  $n_c$ . (b) Same as panel (a) but for  $\beta = 100$ . (c) The difference between the exact wavenumber of maximum growth  $n_{\max}$  and the approximate wavenumber of maximum growth  $n_c$  as a function of the supercriticality  $\mu$ . (d) The relative difference between the exact growth rate  $\sigma$  for a jet at wavenumber  $n_c$  and the approximate growth rate  $\mu^2/c_1$  as a function of supercriticality  $\mu$ . (e) The exact growth rate of jet perturbations with wavenumbers  $\nu_e$  and  $-\nu_e$  as a function of  $\beta$  for supercriticality  $\mu = 0.5$ . The parabolic approximation predicts zero growth for these marginal wavenumbers.



1204 FIG. 5. The amplitude  $\mu A$  of the equilibrated most unstable jet with wavenumber  $n_c$  as a function of super-  
 1205 criticality  $\mu$  for four values of  $\beta$ . The G–L branch is shown with circles  $\bigcirc$ ; the upper branch (which appears for  
 1206  $\beta \gtrsim 20$ ) is shown with triangles  $\triangle$ . Solid lines show the jet amplitude as predicted by the G–L (cf. (29)).



1207 FIG. 6. The bifurcation diagram for  $\beta_{58}$  (case shown in panel (c) of Fig. 5). (a) The amplitude  $\mu A$  of the  
 1208 equilibrated most unstable jet with wavenumber  $n_c$  as a function of the energy input rate. Squares denote the  
 1209 homogeneous equilibrium, circles the lower branch predicted by the G–L dynamics and the triangles the upper  
 1210 branch of equilibria. Open symbols denote unstable jet equilibria with respect to S3T dynamics; filled symbols  
 1211 denote stable jet equilibria. Multiple stable equilibria exist for  $0.89 \leq \varepsilon/\varepsilon_c \leq 1.068$ . A comparison of the jet  
 1212 equilibrium structure and the jet spectra for  $\varepsilon = 1.0025$  (which corresponds to  $\mu = 0.05$ ) is shown in panels  
 1213 (b)–(d). Panels (b), (d) show the lower G–L branch jet; Panels (c), (e) show the upper branch jet. In panel (d) the  
 1214 amplitude prediction for  $n_c$  by (29) and for  $2n_c$  by (22a) is also shown (open circles).



1215 FIG. 7. The amplitude  $\mu A$  of the equilibrated unstable jets with wavenumbers  $n_c - 1/(\mu k_{f*} L_*)$  (diamonds)  
 1216 and  $n_c + 1/(\mu k_{f*} L_*)$  (squares) as a function of supercriticality  $\mu$  for four values of  $\beta$ . The dashed lines show  
 1217 the amplitude predicted by the G–L dynamics (cf. (29)), while the solid lines show the amplitude predicted by  
 1218 the G–L dynamics with  $c_2^{\text{ex}\pm}$  as described in the text. Stable (unstable) equilibria are denoted with filled (empty)  
 1219 symbols and the vertical dotted lines show the stability boundary (58) obtained from the G–L dynamics (see  
 1220 section 7).

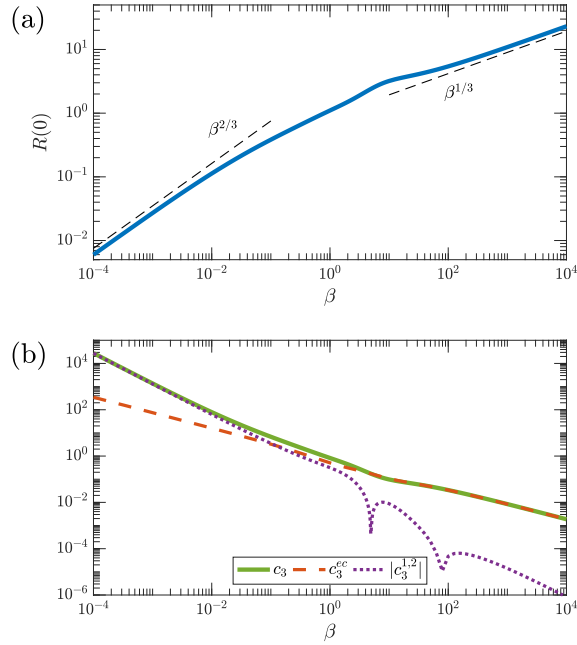
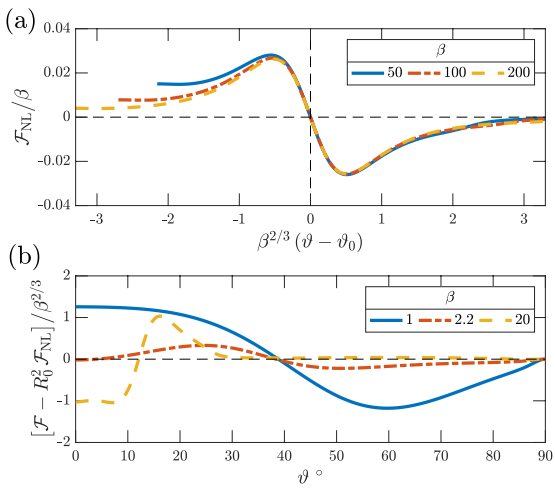


FIG. 8. (a) The amplitude  $R_0(0) = 1/\sqrt{c_3}$  of the equilibrated most unstable jet with wavenumber  $n_c$  as a function of  $\beta$ . Dashed lines show the  $\beta^{1/3}$  and  $\beta^{2/3}$  slopes for reference. (b) The coefficient  $c_3$  and its decomposition into the contributions  $c_3^{ec}$  and  $c_3^{1,2}$  as a function of  $\beta$ . Coefficient  $c_3^{1,2}$  is negative for  $4.9 \lesssim \beta \lesssim 79$ . However, for these values of  $c_3^{1,2}$  is at least an order of magnitude less than  $c_3^{ec}$  and, therefore, negligible.



1225 FIG. 9. (a) The contribution  $\mathcal{F}_{\text{NL}}$  to the coefficient  $c_3$  from waves at angle  $|\vartheta|$  in the limit of  $\beta \gg 1$ .  $\mathcal{F}_{\text{NL}}$   
1226 assumes a dipole pattern. The amplitude of each of the dipole peaks scale with  $\beta$  and the widths of the dipole  
1227 structure scale with  $\beta^{-2/3}$ . For  $\beta \gg 1$  the structure of  $\mathcal{F}_{\text{NL}}$  is independent of the type of forcing used. (b) The  
1228 contribution from waves at angle  $|\vartheta|$  to the finite amplitude equilibrium jet, as given by  $\mathcal{F} - R_0^2 \mathcal{F}_{\text{NL}}$  for three  
1229 values of  $\beta$ .

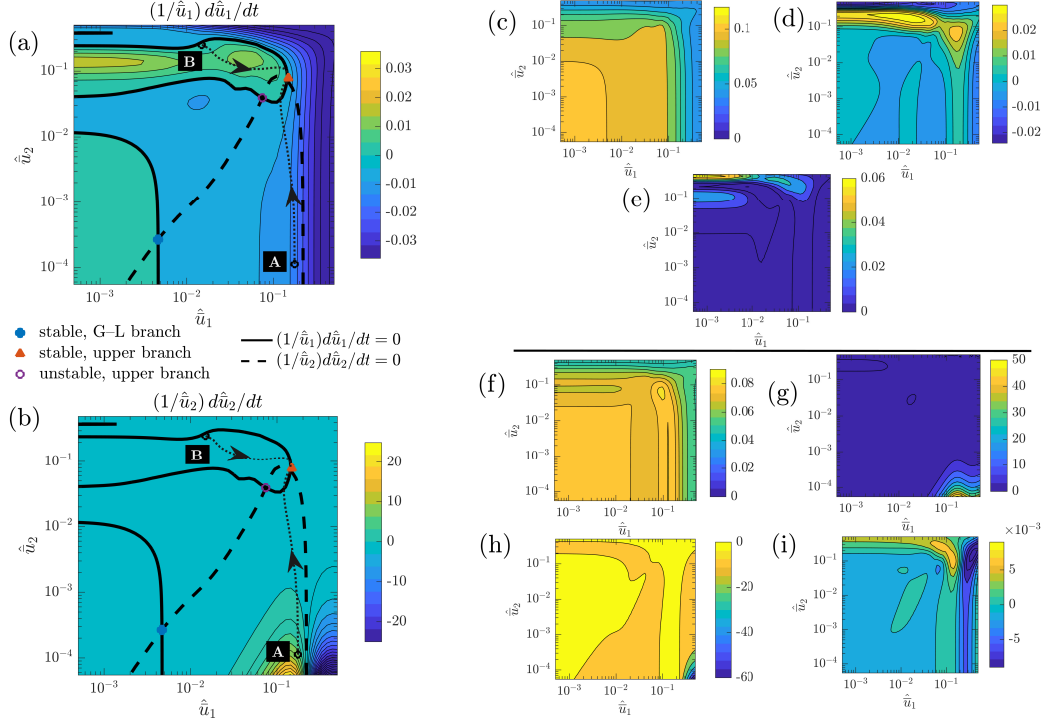
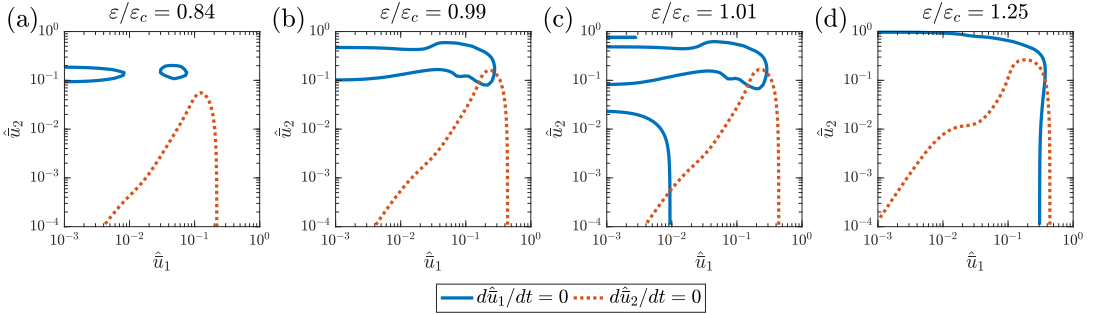
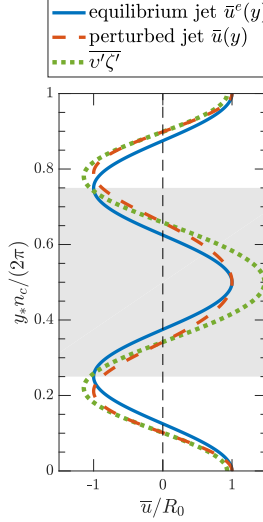


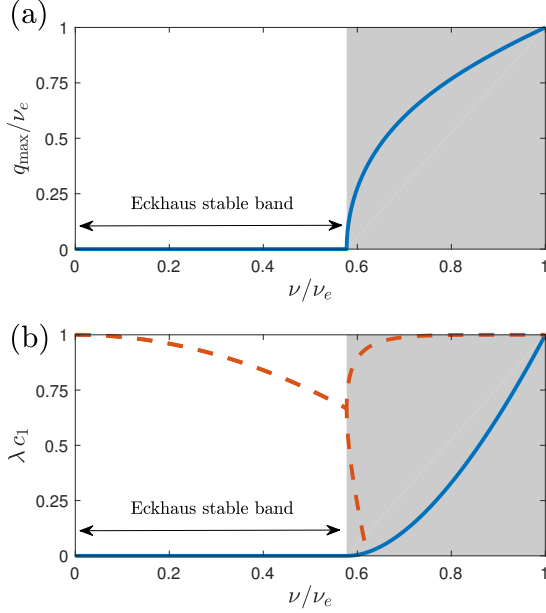
FIG. 10. The mean flow growth rates  $(1/\hat{u}_1)d\hat{u}_1/dt$  (panel (a)) and  $(1/\hat{u}_2)d\hat{u}_2/dt$  (panel (b)) obtained under an adiabatic approximation ( $\partial_t C = 0$ ) for a mean flow  $\bar{u} = \hat{u}_1 e^{in_c y} - \hat{u}_2 e^{2in_c y}$  as a function of  $\hat{u}_1$  and  $\hat{u}_2$ . The thick curves are the zero tendency contours (solid curve for the  $d\hat{u}_1/dt$  and dashed for  $d\hat{u}_2/dt$ ). Infinitesimal jet perturbations start in the region in the  $\hat{u}_1-\hat{u}_2$  phase space denoted as G-L and end up in the lower branch equilibrium shown by the filled circle. The arrows denote paths in the  $\hat{u}_1-\hat{u}_2$  phase space that connect a finite amplitude jet perturbation starting from points A and B and ending up to the upper branch equilibrium, denoted by the filled triangle. (The paths were obtained by time-stepping the S3T system (5).) Panels (c)–(e) show the breakdown of the flux feedback  $\hat{f}_{n_c k_f^*}/\hat{u}_1$  into the components (c)  $f_{1,0}/\hat{u}_1$ , (d)  $f_{1,2}/\hat{u}_1$  and (e)  $f_{2,3}/\hat{u}_1$ . Similarly, panels (f)–(i) show the breakdown of  $\hat{f}_{2n_c k_f^*}/\hat{u}_2$  into the components (f)  $f_{2,0}/\hat{u}_2$ , (g)  $f_{1,1}/\hat{u}_2$ , (h)  $f_{1,3}/\hat{u}_2$  and (i)  $f_{2,4}/\hat{u}_2$ . Parameters used:  $\beta_{58}$  and supercriticality  $\mu = 0.1$ .



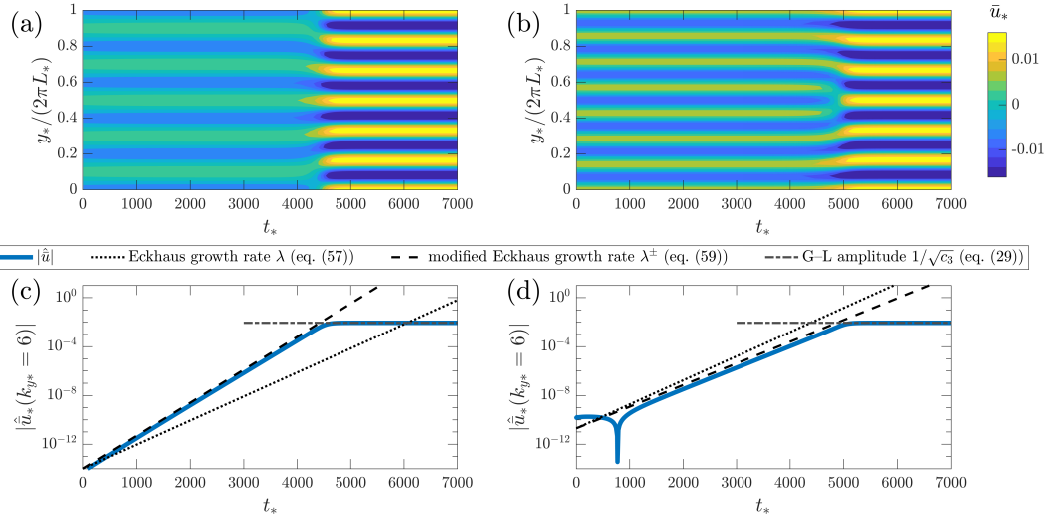
1240 FIG. 11. The locus of zero mean flow tendencies in  $\hat{u}_1$ – $\hat{u}_2$  space for various supercriticalities for the case  
 1241 with  $\beta_{58}$ . Jet equilibria exist at the intersection of the two loci, when  $d\hat{u}_1/dt = d\hat{u}_2/dt = 0$ . For (a)  $\varepsilon/\varepsilon_c = 0.84$   
 1242 there is no intersection as only the homogeneous equilibrium is stable for  $\varepsilon/\varepsilon_c < 0.89$  (see Fig. 6(a)). For (b)  
 1243  $\varepsilon/\varepsilon_c = 0.99$  there are two points of intersection that correspond to the stable and unstable upper branch equilibria  
 1244 that exist for  $0.89 < \varepsilon/\varepsilon_c < 1$ . For (c)  $\varepsilon/\varepsilon_c = 1.01$  there are three equilibria: two upper-branch equilibria (a stable  
 1245 and an unstable) and the lower-branch G–L equilibrium. For (d)  $\varepsilon/\varepsilon_c = 1.25$  only one upper branch equilibrium  
 1246 exists as the G–L branch and the unstable upper branch terminate at  $\varepsilon/\varepsilon_c = 1.068$ .



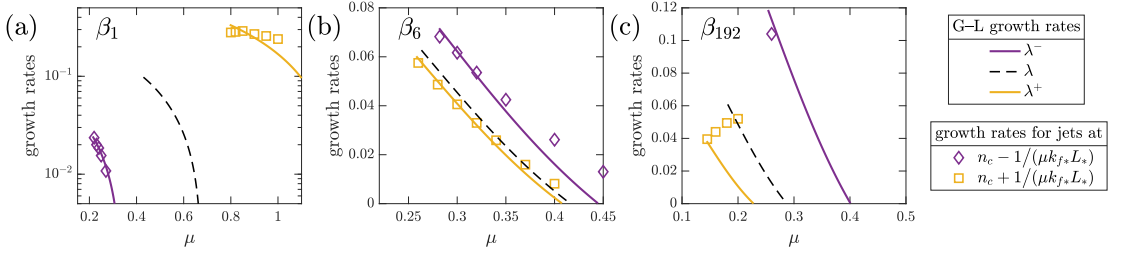
1247 FIG. 12. Solid curve shows a sinusoidal equilibrium jet  $\bar{u}^e = R_0 \cos [(n_c + \mu v)y]$  with smaller scale ( $v = n_c$ )  
 1248 compared to the scale of the most unstable jet (we take  $\mu = 1$  so that the wavenumber differences with the most  
 1249 unstable jet are exaggerated for illustration purposes). Dashed curve shows the resulting jet when the phase of  
 1250 the equilibrium jet  $\bar{u}^e$  is perturbed:  $\bar{u} = R_0 \cos [(n_c + \mu v)y + \eta \sin(qy)]$ , with  $q = v$  and  $\eta = 1/2$  (for illustration  
 1251 purposes). This perturbation dilates the jet in the shaded region and compresses the jet in the unshaded region.  
 1252 Dash-dotted curve is a qualitative depiction of the expected vorticity flux feedback  $\bar{v}'\zeta'$  for the perturbed jet  
 1253 based on the dependence of  $f_r$  on the wavenumber  $v$ .



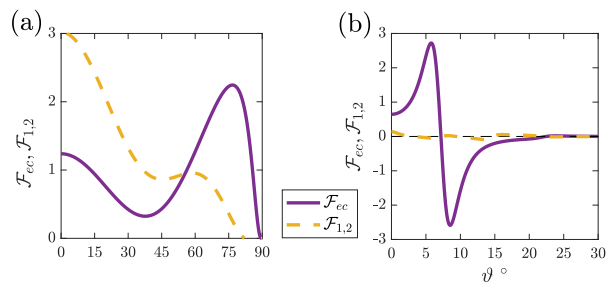
1254 FIG. 13. (a) The most unstable wavenumber for the Eckhaus instability,  $|q|_{\max}/v_e$ , as a function of the  
 1255 jet equilibrium wavenumber  $v/v_e$ . Instability occurs in the shaded region for  $v/v_e > 1/\sqrt{3}$ . (b) The growth  
 1256 rate for the most Eckhaus unstable jet with  $q = q_{\max}$  (57) as a function of the jet equilibrium wavenumber  $v$   
 1257 (solid line). Also shown with dashed line is the corresponding growth rate for the flow-forming instability of  
 1258 the jet with wavenumber  $v \pm q_{\max}$  that will eventually be formed by the Eckhaus instability and is given by  
 1259  $[1 - (v \pm q_{\max})^2/v_e^2]/c_1$ , according to the G–L equation (27).



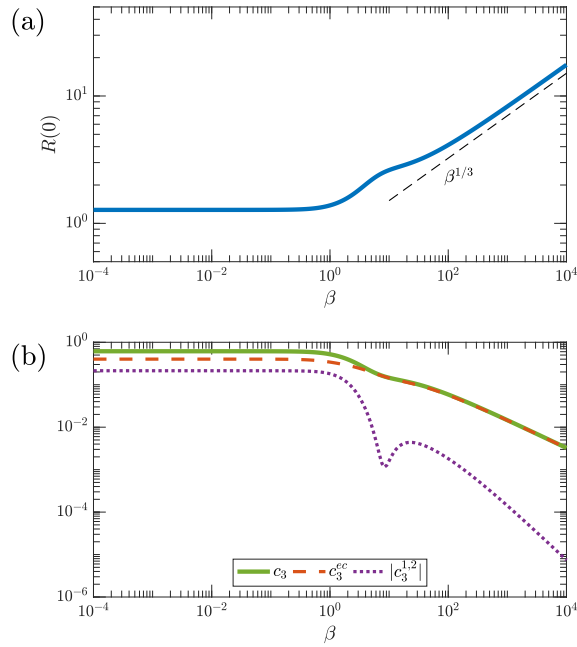
1260 FIG. 14. The equilibration of the Eckhaus instability under S3T dynamics. Panel (a) shows the evolution  
 1261 of the mean flow,  $\bar{u}_*(y, t)$ , for the slightly perturbed  $n_* = 5$  ( $v^-$ ) equilibrium. Panel (c) shows the evolution of  
 1262 the  $n_* = 6$  Fourier component of the flow (solid). Also shown in panel (b) are the growth rate predicted by (59)  
 1263 (dashed) and the amplitude of the  $n_* = 6$  jet as predicted by (29) (dash-dot). Panels (b) and (d) show the same but  
 1264 for the slightly perturbed  $n_* = 7$  ( $v^+$ ) equilibrium. The planetary vorticity gradient is  $\beta_6$  and the supercriticality  
 1265 is  $\mu = 0.3$ .



1266 FIG. 15. Growth rate for the Eckhaus instability of the finite amplitude jets. Shown is the growth rate as  
 1267 a function of supercriticality  $\mu$  for three values of  $\beta$  obtained from the stability analysis for the equilibrium  
 1268 jets with wavenumbers  $n_c - 1/(\mu k_{f*} L_*)$  (diamonds) and  $n_c + 1/(\mu k_{f*} L_*)$  (squares) using the fully nonlinear  
 1269 system (5). Dashed curves show the growth rate as predicted from the G–L dynamics; Solid curves show the  
 1270 growth rate (59) as predicted from the G–L dynamics using the modified values for  $c_2$ , while dashed curves  
 1271 show the unmodified growth rate (D4).



1272 FIG. 16. The contribution of the two feedbacks  $\mathcal{F}_{ec}$  (solid) and  $\mathcal{F}_{1,2}$  (dashed) to the nonlinear coefficient  
 1273  $\mathcal{F}_{NL}$ . Panel (a) shows the case with  $\beta = 0.1$  while panel (b) with  $\beta = 100$ .



1274 FIG. 17. Same as Fig. 8 but for anisotropic forcing with  $\gamma = 1$ . (a) The amplitude  $R_0(0) = 1/\sqrt{c_3}$  of the  
 1275 equilibrated most unstable jet with wavenumber  $n_c$  as a function of  $\beta$  for the case with isotropic ( $\gamma = 0$ ) and  
 1276 anisotropic ( $\gamma = 1$ ) forcing. Dashed line show the  $\beta^{1/3}$  slope for reference. (b) The coefficient  $c_3$  and its  
 1277 decomposition into the contributions  $c_3^{ec}$  and  $c_3^{1,2}$  as a function of  $\beta$ .